Comparison of the Tornadic and Nontornadic Supercells Intercepted by VORTEX2 on 10 June 2010

Alicia M. Klees, Yvette P. Richardson, and Paul M. Markowski

The Pennsylvania State University, University Park, Pennsylvania

Christopher Weiss

Texas Tech University, Lubbock, Texas

Joshua M. Wurman and Karen K. Kosiba

Center for Severe Weather Research, Boulder, Colorado

ABSTRACT

On 10 June 2010, the second Verification of the Origins of Rotation in Tornadoes Experiment (VORTEX2) armada collected a rare set of observations of a nontornadic and a tornadic supercell evolving in close proximity to each other. The storms and their environments were analyzed using single- and dual-Doppler radar, mobile mesonet, deployable surface mesonet, and mobile sounding data, with the goal of understanding why one supercell produced no tornadoes while the other produced at least two. Outflow temperature deficits were similar for the two storms, both within the normal range for weakly tornadic supercells but somewhat cold relative to significantly tornadic supercells. The storms formed in a complex environment, with slightly higher storm-relative helicity near the tornadic supercell. The environment evolved significantly in time, with large thermodynamic changes and increases in storm-relative helicity, leading to conditions much more favorable for tornadogenesis. After a few hours, a new storm developed between the supercells, likely leading to the demise of the nontornadic supercell before it was able to experience the enhanced environmental conditions. Two tornadoes developed within the single mesocyclone of the other supercell. After the dissipation of the second tornado, rapid rearward motion of low- to midlevel circulations may have inhibited further tornado production in this storm.

1. Introduction

Tornadoes are dangerous, often highly destructive phenomena that can threaten life and/or property. The tornado outbreak of 25–28 April 2011 alone killed 321 people and caused billions of dollars in damage (NOAA 2011). Currently, forecasters can sometimes predict with accuracy hours to days in advance if such tornado outbreaks will occur, as was the case in April 2011. However, determining which particular supercells will generate tornadoes is a serious challenge; nontornadic and tornadic supercells alike can have significant low-level rotation on the mesocyclone scale (Markowski et al. 2011), and the majority of supercells never produce tornadoes (Trapp et al. 2005). Increasing our understanding of the differences in the environments and internal processes and characteristics of nontornadic and tornadic supercells is, therefore, crucial to better forecasting.

The second Verification of the Origins of Rotation in Tornadoes Experiment (VORTEX2) was designed to study such processes and environmental characteristics by collecting wind (radar) and thermodynamic (sounding, mobile mesonet, and deployable mesonet) observations within tornadic and nontornadic supercells (Wurman et al. 2012) and their environments. Given that synoptic-scale forcing can vary substantially from case to case, it can be difficult to compare tornadic and nontornadic supercells across different days. The optimal observational approach
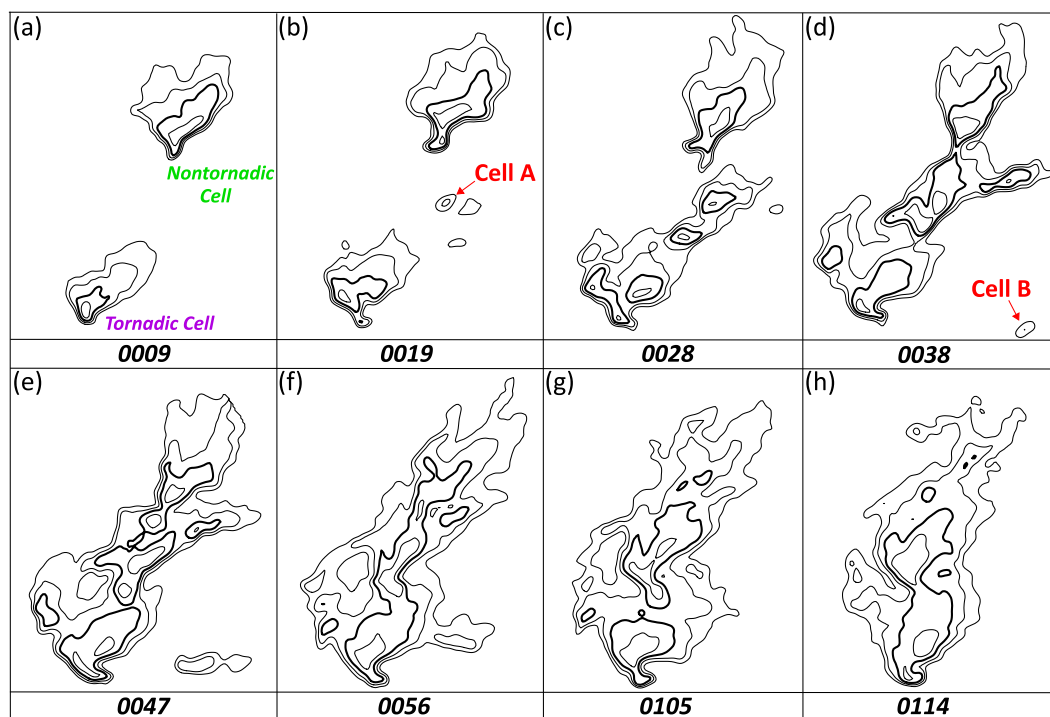
FIG. 1. Progression of interactions between original cells and cells A and B (indicated in red). Contours are of KFTG WSR-88D logarithmic equivalent reflectivity factor Z_e, every 10 dBZ beginning at 25 dBZ (with the 45-dBZ contour thickened), at heights of 1.5 km (0009–0047 UTC) or 2.0 km (0056–0114 UTC).

to do so, therefore, may be to examine supercells occurring in the same region on the same day. The VORTEX2 armada collected a rare dataset like this on 10 June 2010, when it deployed on one nontornadic and one tornadic supercell evolving in close proximity to each other in northeastern Colorado (Fig. 1). The VORTEX2 armada intercepted the northern of the two supercells, which was never tornadic, from 2345 to 0040 UTC, before redeploying to intercept the more impressive supercell to the south from 0110 to 0230 UTC (Fig. 2). This southern storm generated two tornadoes from 0109 to 0115 UTC and 0122 to 0126 UTC, respectively; the two tornadoes were weak [enhanced Fujita (EF0) rating according to *Storm Data* (NCDC 2010)], and no damage was found in a survey performed by Lyndon State University (N. Atkins 2015, personal communication). To examine why one storm produced no tornadoes and the other produced two, we investigate the storms' interactions with other cells, as well as the storms' environments and kinematic fields. We study the tornadic supercell's tornado production, as the tornadoes are the crucial distinguishing factor between the two storms. We also examine the tornadic supercell's subsequent mesocyclone behavior, as it may have inhibited further tornado production in this storm.

To understand how environmental characteristics influence tornado potential, we first briefly review the

current understanding of the genesis and maintenance of tornadoes associated with a mesocyclone (i.e., ignoring nonmesocyclonic tornadoes such as landspouts). To produce a tornado, a supercell must 1) generate rotation (a mesocyclone) at midlevels, 2) generate rotation near the surface, and 3) significantly strengthen rotation near the surface (Davies-Jones 2015). The first step is well understood and occurs when an updraft [whose strength, at least the part owing to buoyancy, depends on the convective available potential energy (CAPE)] tilts and stretches horizontal vorticity associated with the mean vertical wind shear in the environment (Rotunno 1981; Lilly 1982; Davies-Jones 1984). If the horizontal vorticity is mostly streamwise (i.e., if the environmental vorticity vector is nearly parallel to the horizontal storm-relative winds) and the storm-relative winds are sufficiently strong ($>10 \, \mathrm{m \, s^{-1}}$), then the result is cyclonic vertical vorticity nearly collocated with the updraft (i.e., a cyclonic midlevel mesocyclone) (Davies-Jones 1984). Storm-relative helicity over the inflow layer (taken to be the lowest 3 km) measures the combination of streamwise vorticity and the strength of the storm-relative winds [hereafter, storm-relative helicity (SRH) between 0 and 3 km is denoted SRH3].

However, the tilting of horizontal vorticity by the updraft will not generate vertical vorticity very close to the surface,
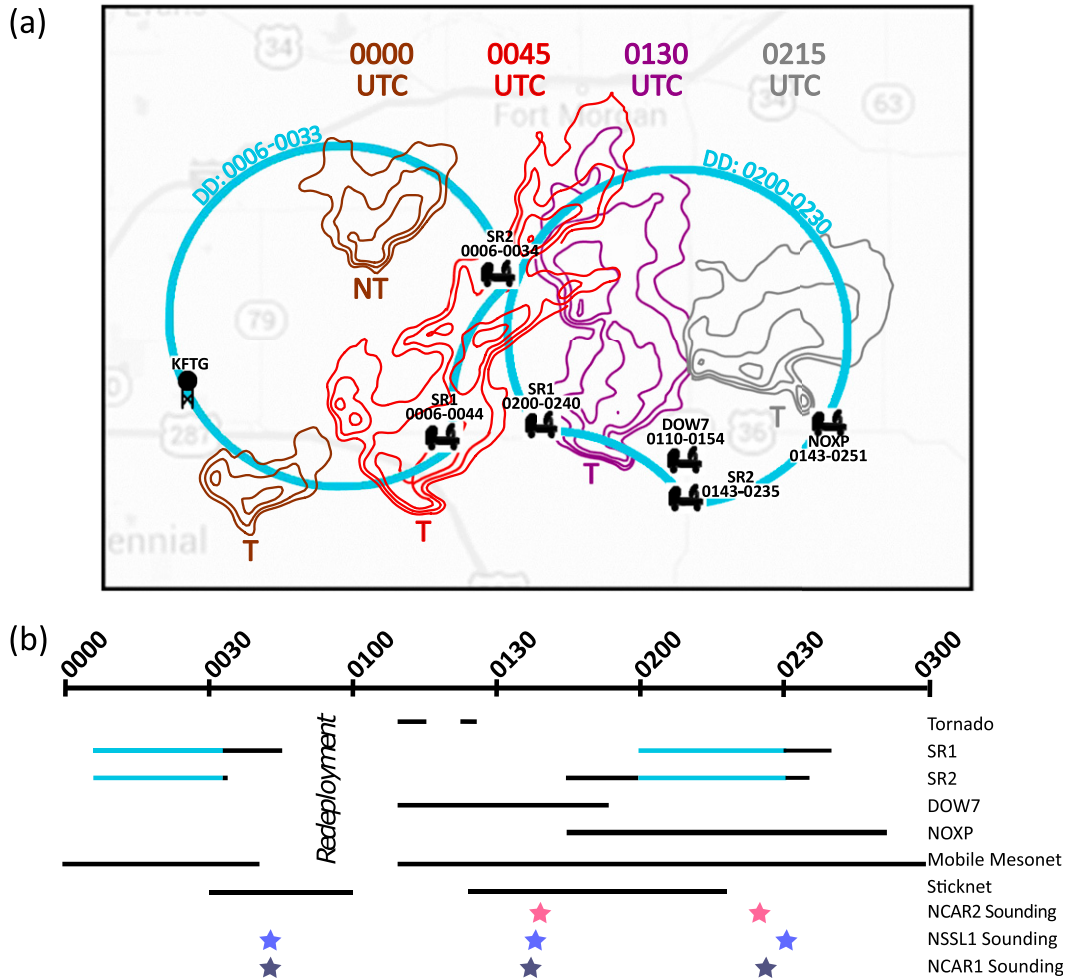
FIG. 2. (a) Deployment map for 10 Jun 2010. The Z_e contours from the KFTG radar are shown every 45 min for the nontornadic (northern) and tornadic (southern) supercells. Radar truck icons show the location of each mobile radar deployment, with time ranges indicated. The stationary radar icon denotes the location of the KFTG WSR-88D radar. Dual-Doppler lobes are outlined in blue, with dual-Doppler time periods noted. VORTEX2 deployed on the nontornadic supercell first (2345–0040 UTC) and then the tornadic supercell (0110–0230 UTC). (b) Timeline of instrument deployments during the main analysis periods, with dual-Doppler time periods indicated in blue. Additional soundings were launched prior to the radar deployments and are not shown in the timeline.

as the updraft advects the vorticity away from the ground as it is produced. Thus, a downdraft is crucial for developing near-surface rotation if none preexists the storm. Current theories suggest the downdraft tilts horizontal vorticity that is baroclinically (or possibly frictionally) generated in the outflow into the vertical and advects the resulting vertical vorticity toward the surface (Klemp and Rotunno 1983; Rotunno and Klemp 1985; Davies-Jones and Brooks 1993; Davies-Jones 2015; Markowski and Richardson 2014; Dahl et al. 2014; Schenkman et al. 2014). An alternative to the baroclinic or frictional mechanisms was offered by Davies-Jones (2008) who showed that an imposed rain curtain could instigate tornadogenesis, given an initial midlevel mesocyclone, through an enhanced downdraft

that transports moderately high-angular-momentum air toward the surface.

In the final step, the near-surface vertical vorticity must then become collocated with updraft forcing, so it can strengthen through vortex stretching. Vorticity stretching sufficient for tornadogenesis is contingent upon the ability of surface outflow parcels to be lifted, which is most easily accomplished if a strong vertical dynamic perturbation pressure gradient force is present and if the parcels are not too negatively buoyant (Markowski and Richardson 2014).

The strong upward dynamic perturbation pressure gradient force is often associated with rotation aloft, whose strength and distance above the ground determine the magnitude of the pressure gradient (Markowski and

Richardson 2014). The strength of this dynamic lifting has been tied to the 0–1-km storm-relative helicity (SRH1) (Markowski and Richardson 2014), a measure of the low-level environmental streamwise vorticity (Davies-Jones et al. 1990), which is typically higher in tornadic supercell environments than nontornadic supercell environments (Rasmussen 2003; Thompson et al. 2012). Indeed, composite environments created by Parker (2014) for VORTEX2 tornadic and nontornadic supercells, based on targeted VORTEX2 soundings, show increased alignment between the 0–1-km environmental horizontal vorticity and the storm-relative winds in the tornadic cases, although it is not clear that this relationship holds in shallower layers near the surface.

Given these favorable conditions for lifting beneath the mesocyclone, it is reasonable to expect the most likely scenario for tornado formation to involve vertical alignment between the low- and midlevel circulations, with the midlevel circulation also coincident with the buoyant updraft to provide further support for lifting. Skinner et al. (2014) found that the low-level mesocyclone in their observed case intensified and grew upward when aligned with the midlevel mesocyclone, whereas Burgess et al. (1982) describe storm-relative rearward motion of vortices that become separated from the updraft as outflow surges around them to the east, resulting in cyclic behavior as new mesocyclones form at the subsequent occlusion point. Dowell and Bluestein (2002b) link the dissipation of a tornado to its displacement from the midlevel updraft owing to changes in the low-level outflow winds in which it was embedded. Similarly, French et al. (2008) noted significant rearward (with respect to storm motion) advection of pretornadic (i.e., those forming prior to the vortex that became tornadic) vortices, presumably limiting their ability to experience the forcing necessary to become tornadic. The tornadic vortex in their case, in contrast, exhibited much weaker rearward motion. Tanamachi et al. (2012) suggest more similar updraft motion and tornado motion for a long-lived tornado than a short-lived tornado. Marquis et al. (2012) also found that the longest-lived tornado in their study was maintained under the midlevel updraft, but that the shortest-lived tornado was similarly located below the midlevel updraft, suggesting that this vertical alignment, while important, may not always be sufficient for successful tornado maintenance.

Also crucial to lifting are the thermodynamic characteristics of the outflow parcels, with less-negatively buoyant parcels more easily lifted. Measurements made within the outflow of supercells suggest that tornadic supercells tend to have warmer outflows than nontornadic supercells (Markowski et al. 2002; Shabbott and Markowski 2006; Hirth et al. 2008; Weiss et al. 2015). Markowski et al. (2002) found, using mobile mesonet observations, that RFDs in "weakly" tornadic (i.e., producing EF0 or EF1 tornadoes lasting less than 5 min) and nontornadic supercells had maximum virtual potential temperature deficits of 4°–7°C, compared to less than 2°C in significantly tornadic supercells (producing EF2 or greater tornadoes, or tornadoes of any strength lasting greater than 5 min). Markowski et al. (2002) also found equivalent potential temperature deficits in nontornadic supercells of 10°–12°C, compared to less than 4°C in significantly tornadic supercells. The advantage of having outflow that is not too cold is consistent with climatological observations showing that tornadic supercells tend to have a lower environmental lifting condensation level (LCL), indicating higher relative humidity and presumably less evaporation of precipitation (all else being equal), than nontornadic supercells (Rasmussen and Blanchard 1998; Thompson et al. 2012).

Forecasters use the significant tornado parameter (STP) (Thompson et al. 2002, 2003) given by

$$STP = (MLCAPE/1000\,J\,kg^{-1})(6BWD/20\,m\,s^{-1})$$
$$\times (SRH1/100\,m^2\,s^{-2})[(2000 - MLLCL)/1500\,m],$$

where 6BWD is the 0–6-km vertical wind shear (defined here as the magnitude of the vector difference between the winds at a height of 6 km and at the surface), MLCAPE is the mixed-layer CAPE, and MLLCL is the mixed-layer LCL. (Mixed-layer quantities are computed using average parcel properties over the lowest 100 hPa above the surface.) The first two parameters in the STP discriminate well between nonsupercell and supercell environments, whereas the latter two help discriminate between tornadic and nontornadic supercell environments as described above. A STP value of 1 represents "a reasonable guideline to discriminate between significantly tornadic and nontornadic supercells" based on forecast skill scores derived from climatology (Thompson et al. 2003). Unfortunately, the distributions of STP for nontornadic supercells and those producing only weak tornadoes show considerable overlap, making marginal tornado cases more difficult to predict.

One significant complication to the forecasting problem is the potential for spatial heterogeneity of each of these environmental characteristics and the temporal evolution of these quantities over the lifetime of a storm system. Markowski et al. (1998), using soundings from the 1994–95 VORTEX field campaign, showed large spatial variations in storm-relative helicity, particularly for storms occurring in the vicinity of an airmass boundary. Richardson et al. (2007) showed that idealized spatial variations in shear could strongly impact ongoing storm systems that travel through these variations. We might expect mesoscale subregions, likely at scales not well resolved by the operational observing network, to be more

TABLE 1. Radar deployment details.

Storm	Radar	Location relative to mesocyclone	Elev angles used (°)
Nontornadic supercell	SR1	25 km, south	0.5, 1.3, 2.3, 3.3, 4.2, 5.1, 6.1, 7.8, 10.0, 11.9
Nontornadic supercell	SR2	30 km, southeast	0.6, 1.3, 2.0, 2.7, 3.4, 4.1, 4.9, 5.7, 6.5, 7.3, 8.1, 9.3, 10.5, 12.2
Tornadic supercell	SR1	30 km, west	0.5, 1.3, 2.3, 3.3, 4.2, 5.1, 6.1, 7.8, 10.0, 11.9
Tornadic supercell	SR2	25 km, southwest	0.6, 1.3, 2.0, 2.7, 3.4, 4.1, 4.9, 5.7, 6.5, 7.3, 8.1, 9.3, 10.5, 12.2
Tornadic supercell	DOW7	20 km, northeast	0.5, 1.0, 2.0, 3.0, 4.0, 5.0, 6.0
Tornadic supercell	NOXP	15 km, southeast	1.0, 2.0, 3.0, 4.0, 5.0, 6.0, 7.0

favorable for tornadoes. These subregions could develop through many different mesoscale processes including differential heating, mesoscale moisture advection, terrain influences, etc. Similarly, environments can evolve on temporal scales well below those of the observing network. Richardson and Droegemeier (1996), Kost (2004), Letkewicz et al. (2013), and Davenport and Parker (2015) all showed that temporal variations in a storm environment can lead to changes in storm outflow and rotational characteristics compared to a storm staying in the original environment. Coffer and Parker (2015) document large changes in hodograph shape during the early evening transition using soundings from VORTEX2, and use an idealized modeling framework to show these hodograph changes are linked to increases in dynamic lifting that aid the intensification of near-surface vorticity in the presence of increasing low-level stability.

Thus far, we have considered only influences on isolated cells, but often cells do not remain isolated over their entire lifetime. When two storms no longer have separate reflectivity maxima [in this study, based on a threshold of 35 dBZ, per Rogers (2012)], they have officially begun merging. Cell mergers can lead to changes in supercell behavior, including increased tornado production or the demise of the original supercell.

A merger may amplify low-level vertical vorticity, in agreement with some observations of tornadogenesis near the time of cell mergers (Lee et al. 2006; Wurman et al. 2007; Rogers and Weiss 2008). Enhancement of precipitation during a merger alters baroclinic zones and leads to a surge of outflow that can help stretch vorticity to tornado strength (e.g., Finley et al. 2001). In a study over five years, 27% of significant tornadoes occurred within 15 min of a merger event (Rogers 2012), as did 54% of nearly 100 tornadoes over 10 days (Rogers and Weiss 2008). Highlighting the complexity of merger outcomes, the observational study of Tanamachi et al. (2015) found that the 2011 El Reno supercell's updraft weakened leading up to a merger, but the merger then led to the development of updraft pulses, which ultimately increased the vertical vorticity in the supercell. Alternatively, a merger can have adverse impacts, overall, on the supercell. Numerical simulations show that a merging (younger) cell may

change the source of the supercell's inflow, leading to the supercell's demise as it ingests cold air from the young storm's outflow (Hastings and Richardson 2016). We will see this scenario play out for the nontornadic supercell on 10 June.

In this study, we will examine rare data collected on one tornadic and one nontornadic supercell evolving in close proximity to each other to address the overarching question of why one supercell produced no tornadoes on this day while the other produced two. A description of the data and analysis methods is given in section 2. We first examine interactions between the supercells and nearby cells (section 3). We then compare environmental characteristics near the two storms and document the spatial and temporal variability (section 4). We next examine the storms' outflow characteristics and kinematic fields to look for any obvious differences (section 5). Then, we analyze the evolution of the two tornadoes in the tornadic supercell (section 6). Finally, we study the motion of vortices in the tornadic supercell during its ensuing long nontornadic period (section 7). Concluding thoughts are offered in section 8.

2. Data and methods

The VORTEX2 armada collected an extensive dataset on 10 June 2010. For this case study, the focus will be on single-Doppler radar observations from the WSR-88D (KFTG) over the whole time period; from NOAA X-band dual-Polarization radar (NOXP; e.g., Burgess et al. 2010) and the Shared Mobile Atmospheric Research and Teaching (SMART) radars (SR1 and SR2; Biggerstaff et al. 2005) during the late stages of the tornadic storm; two dual-Doppler (using SR1 and SR2) deployments (one on each storm); single-Doppler radar observations from a Doppler on Wheels (DOW7) radar (Wurman et al. 1997) for the tornadic supercell during the two tornadoes; mobile mesonet and sounding data during both storms; and surface meteorological data from StickNet (Weiss and Schroeder 2008; Weiss et al. 2015) during the tornadic supercell (Fig. 2).

a. Radar data

Table 1 lists the mobile radar locations and general elevation angles of their data, whereas the locations are shown

TABLE 2. Parameters used in dual-Doppler syntheses.

Storm	Radars	Baseline (km)	Δx, Δz (km)	Grid altitude (km)	κ (km^2)	d (km)	Storm motion (u, v) (m s^{-1})
Nontornadic	SR1–SR2	33	0.3	1.469	1.43	0.9	9.68, 0.58
Tornadic	SR1–SR2	20	0.3	1.478	1.43	0.9	10.46, 4.94

graphically in Fig. 2. Radar data were edited using the National Center for Atmospheric Research (NCAR) Solo II radar data editing and visualization software (Oye et al. 1995). Four independent estimates of velocity are available for DOW7, which used two different frequencies (9.35 and 9.50 GHz), each having two different pulse repetition times (the long and short pulse of the stagger). For each frequency, a radial velocity estimate is derived using standard staggered-pulse pulse-pair velocity retrieval, and then the resulting two estimates are averaged together to give the final estimated value for that radar gate. Velocities are filtered based on the normalized coherent power (NCP), eliminating velocities for which NCP is below 0.2–0.3 (with some subjectivity). The beam along the center of the tornado often spans both sides of an underresolved tornado, resulting in radial velocity estimates that are inconsistent with one another and a noisy averaged field. When that occurred, those center radial pixels were deleted. For the Smart Radar data, velocities are filtered based on returned power (DM) and spectrum width (SW), eliminating velocities for which DM is below around -88 dBZ and/or SW exceeds 8–10 m s^{-1} (with some subjectivity). For all radars, data believed to result from sidelobe contamination, ground clutter, etc., were removed separately. Of particular note, the SR1 elevation angles were corrected by approximately $-1.5°$ using the azimuth-dependent correction equation in Rilling and Schumacher (2013), who originally identified this angle offset in SR1 data collected during the Dynamics of the Madden–Julian Oscillation (DYNAMO) experiment in 2011–12. Our independent analysis of reflectivity features from different radars suggest this offset must be applied to our VORTEX2 data as well, although we do not know if this applies to data collected earlier in the VORTEX2 project.

Edited radar data were objectively analyzed to a Cartesian grid using the two-pass Barnes successive corrections method (Barnes 1964; Koch et al. 1983; Majcen et al. 2008). An isotropic Barnes weighting function was used within this method to retain scales appropriate for the data spacing δ, approximated as $\delta = r\theta$, where r is the radial distance from the radar and θ is the beamwidth. For the first pass, the smoothing parameter κ was set to $(1.33d)^2$, as recommended by Pauley and Wu (1990), where d is the largest value of δ within the analysis domain (Trapp and Doswell 2000). For the second pass, κ was set to $0.3(1.33d)^2$ (Majcen

et al. 2008). The cutoff radius used in gridding the data was $R_c = 3d$. No extrapolation was permitted in the gridding process.

The spacing of the Cartesian grid was set to $\Delta x = \Delta y = \Delta z \approx d/3$, per Koch et al. (1983). The altitude of the grid origin was approximately the average elevation of the ground. The position of the midlevel (2.25 and 1.7 km AGL for the first and second storms, respectively) mesocyclone in the KFTG WSR-88D data was used as the grid origin at each volume time. Midlevel mesocyclone motion was used to correct the position of data to a common reference time for each volume. This advection correction helped reduce an artificial tilt with height of features in the storm due to the temporal offset between data at the beginning of the volume and data at the end.

Radial velocities were synthesized in regions where the between-beam angle was between 30° and 150°. The three-dimensional wind field was obtained by applying an upward integration (assuming $w = 0$ at the surface) of the anelastic mass continuity equation and making iterative adjustments (Brandes 1977; Dowell and Shapiro 2003) to all three wind fields (u, v, and w) until $\Delta(\overline{\rho}w) < 0.01$ kg m^{-2} s^{-1}, [$\overline{\rho}(z)$ being a particular height's reference density], indicating the solution converged. Although extrapolation is not allowed in the gridding stage, we did allow downward extrapolation (from a height of no more than 900 m) of the u and v estimates to facilitate integration of mass continuity. After the final u, v, and w were obtained at all levels, winds were removed from the extrapolated levels so they were not used in analyses.

For both storms, dual-Doppler syntheses were completed using 3-min volumes from SR1 and SR2, for 0006–0033 UTC for the nontornadic supercell and 0200–0230 UTC for the tornadic supercell. Details of the dual-Doppler analyses are summarized in Table 2. In addition to standard kinematic fields such as divergence and vorticity, other quantities derived from the dual-Doppler syntheses include updraft mass flux and circulation. Circulation ($\Gamma = \oint \mathbf{v} \cdot d\mathbf{l}$) was calculated around a 1-km circle centered on the vortex of interest. Average updraft mass flux [$= \sum \rho w / A$; Lebo and Morrison (2014)] was calculated over an area A encompassing the updraft and was summed over all grid points having vertical velocity $w \gtrsim 10$ m s^{-1}.

b. Sounding data

On 10 June 2010, four mobile GPS Advanced Upper-Air Sounding (MGAUS) systems from the National Severe
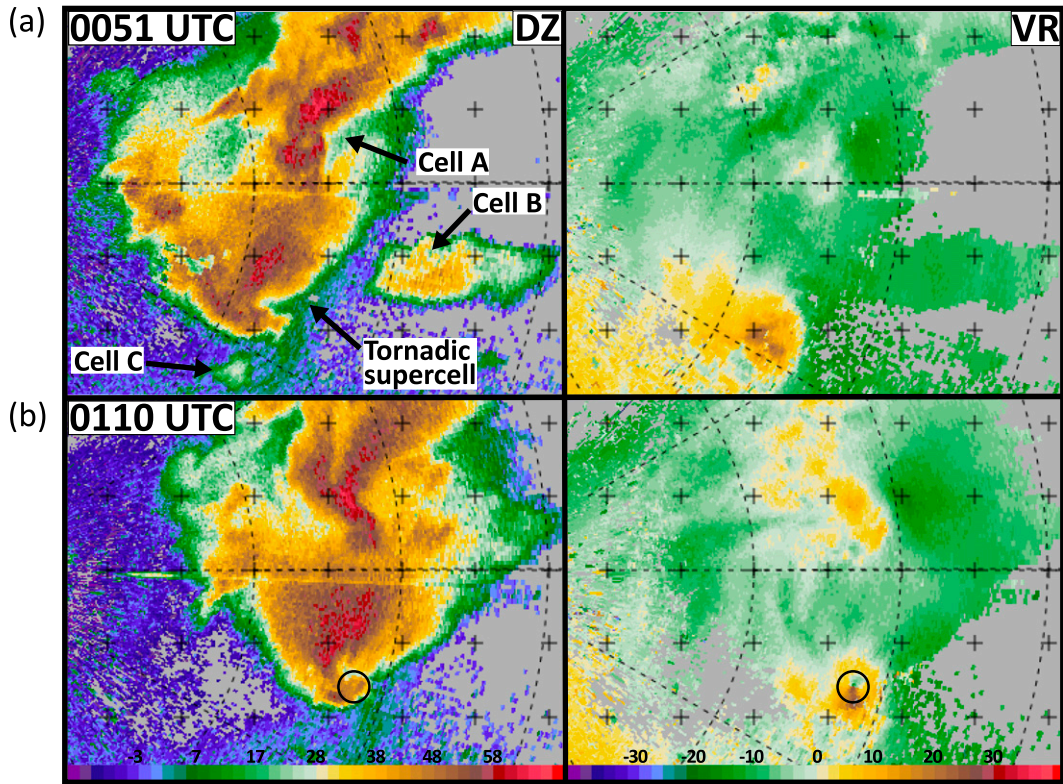
FIG. 3. KFTG WSR-88D (left) Z_e (dBZ) and (right) radial velocity (m s^{-1}) at (a) 0051 and (b) 0110 UTC. Cells A, B, and C are denoted in (a). Tornado is circled in (b).

Storms Laboratory (NSSL) and NCAR were operated by teams from North Carolina State University and NCAR to launch 21 radiosondes in northeastern Colorado, measuring pressure, temperature, relative humidity, and wind velocity every second. Data were quality controlled according to the methods of Loehrer et al. (1996, 1998).

Six radiosondes were launched prior to the storms (we use those launched after ~ 2230 UTC) to measure the existing environmental variability. Once the target storms were identified and the VORTEX2 armada deployed, 15 radiosondes were launched in groups of 3–4 at around 2345, 0040, 0140, and 0230 UTC to sample the mesoscale environment. Within each group, one sounding was launched behind the target storm, with two to three soundings ahead of the target storm in an approximately north–south or northwest–southeast line. These soundings are used to characterize the spatial gradients and temporal evolution of the environment.

Hodographs constructed from the raw sounding data were extremely noisy; thus, we applied smoothing in a manner similar to Parker (2014). In particular, we used a one-pass Barnes (1964) filter with $\kappa = 6.25 \times 10^{-4}$ km^2 within the lowest 1500 m and $\kappa = 2.5 \times 10^{-3}$ km^2 over the rest of the sounding. The smaller κ at lower levels was used to retain as much detail as practical in this layer.

In addition to examining the individual sounding characteristics, the radiosonde data were used to help characterize the environments in which the supercells evolved in a bulk sense. For each sounding, numerous thermodynamic and kinematic parameters, as well as composite indices, were calculated and analyzed, such as MLCAPE,[1] 6BWD, SRH1, SRH3, MLLCL, and fixed-layer STP.

c. Mobile mesonet data

On 10 June 2010, six Pennsylvania State University–NSSL mobile mesonet vehicles with mounted instruments (Straka et al. 1996; Waugh and Fredrickson 2010) were deployed. The first supercell was sampled from 2345 to 0040 UTC, with spatial data coverage in both the forward and rear flanks of the storm. The second supercell was sampled from 0110 to 0230 UTC. Extensive data collection during the two tornadoes was hindered by a sparse road

---

[1] As some soundings were prematurely cut off prior to reaching their equilibrium level, data at higher levels from the 2342 UTC sounding were used so that contributions to CAPE at upper levels could be estimated. This sounding was chosen based on a comparison of all full-depth soundings during the analysis period. The 2342 UTC sounding reasonably represented the general upper-level conditions.
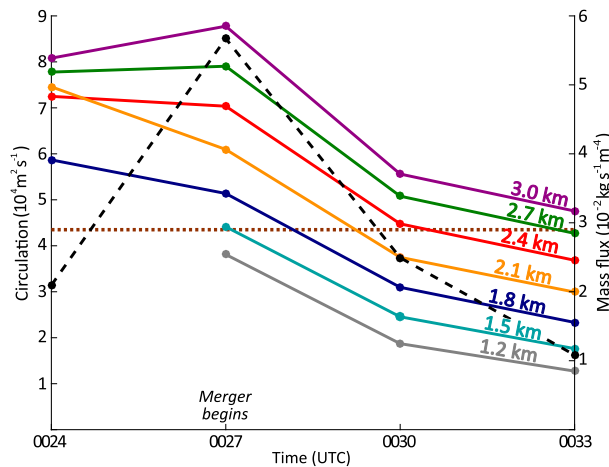
FIG. 4. Impacts of the merger with cell A on characteristics of the nontornadic supercell, in terms of the time evolution of updraft strength at 2.1 km (average updraft mass flux, dashed black curve; 10^{-2} kg s^{-1} m^{-4}) and mesocyclone strength (maximum circulation at a radius of 1 km, various heights denoted by colored solid curves; 10^4 m^2 s^{-1}). The brown dotted line denotes the maximum circulation in the tornadic supercell (based on the times when dual-Doppler data were available) at 1.2 km.

network and the inability to redeploy crews in time, especially during the first tornado. Data sampling improved following the second tornado as teams made their way deeper into the storm.

The mobile mesonet instrumentation collected GPS position, temperature, relative humidity, pressure, and wind velocity data every second. The "U tube" temperature shield design was used, allowing us to retain data from stationary mobile mesonet vehicles (Waugh and Fredrickson 2010) (unlike past studies using the "J tube" design), owing to the superior aspiration of the U-tube shield. Data were checked to remove obvious outliers and unreasonable values. For specifications of the mobile mesonet instruments, potential errors, and quality control procedures, refer to Straka et al. (1996), Markowski et al. (2002), and Waugh and Fredrickson (2010).

Two passes of a triangular weighting filter (using data within 10 s on either side) were applied to the mobile mesonet data to remove high-frequency noise, in effect smoothing the data. In total, 6 min of mobile mesonet data were used in each analysis (i.e., the storm was assumed to maintain a steady state over a 6-min period), with a time–space conversion done to produce analyses valid at a given reference time as in Markowski et al. (2002), Shabbott and Markowski (2006), and Markowski et al. (2012).

For each analysis, virtual potential temperature and pseudoequivalent potential temperature (Bolton 1980) were calculated and used to evaluate the thermodynamic characteristics within and near the supercells relative to a base state. The base state was calculated using observations

collected by the mobile mesonet as the fleet approached the storms, for 15 min prior to deployment.

d. StickNet data

A spatially extensive StickNet dataset was collected during the posttornadic phase of the second storm. From 0142 to 0154 UTC, 17 StickNets were deployed predominantly in a north–south line, with a few in an adjacent east–west line, and captured thermodynamic and wind data as the storm passed over. Only data from 15 StickNets were used in our analyses, as two platforms collected temperature and relative humidity data that appeared unrepresentative when compared against other nearby StickNets over the same time period. Processing/filtering was applied in a similar fashion as with the mobile mesonet data (e.g., using a 6-min steady-state assumption). Note that while StickNet and mobile mesonet data must be compared with caution owing to their different time constants (Skinner et al. 2010), in this study, mobile mesonet and StickNet measurements in close proximity were generally consistent (within 1°C of each other), except in regions having strong gradients, where they differed by up to 2°–3°C. For further details on StickNet data, especially quality control procedures, refer to Weiss et al. (2015) and Skinner et al. (2011).

3. Cell interactions

On 10 June 2010, the nontornadic and tornadic supercells occurred in a region of low CIN conducive to formation of additional cells. Here, we investigate the ensuing interactions between the supercells and some of these younger cells. Both supercells interacted with a new storm that developed between them (hereafter referred to as "cell A") and a small fast-moving reflectivity feature (presumed to be a very young cell, "cell B") (Fig. 1). The tornadic supercell also seemed to interact with a small flanking line cell ("cell C") (Fig. 3a). The merger of the nontornadic supercell with cell A was associated with the nontornadic supercell's demise.

By 0014 UTC, cell A had initiated between the nontornadic and tornadic supercells (Fig. 1), near the intersection of their gust fronts (not shown). Over time, cell A intensified, increased in size, and began merging with the nontornadic supercell (Figs. 1b–e). Dual-Doppler analyses indicate general weakening of the updraft and mesocyclone in the nontornadic supercell during the merger. Updraft mass flux decreased from 0027 UTC onward (Fig. 4). Similarly, analyzed mesocyclone strength, measured in terms of circulation (at a radius of 1 km), decreased significantly from 0027 to 0033 UTC, dropping by at least 20 000 m^2 s^{-1} over this time period at various heights (Fig. 4).
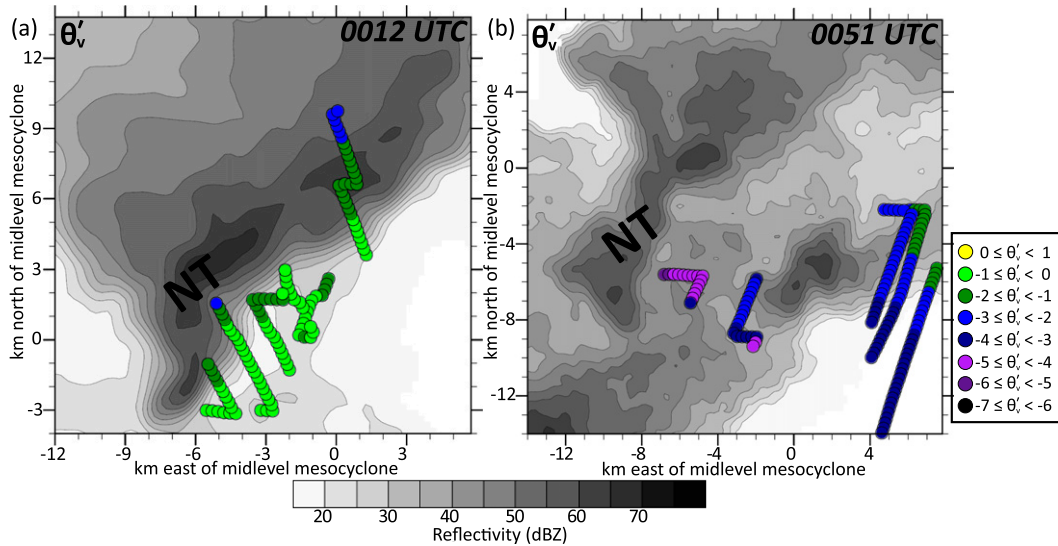
FIG. 5. Mobile mesonet–measured virtual potential temperature perturbations (color-coded circles, relative to base state of 315.9 K) in the inflow region of the nontornadic supercell at (a) 0012 UTC, overlaid on 750-m objectively analyzed SR2 Z_e (dBZ, shaded contours) and (b) 0051 UTC, overlaid on 1.2-km KFTG-88D objectively analyzed Z_e (dBZ, shaded contours).

The weakening of the updraft and mesocyclone of the nontornadic storm during the merger was associated with 1) inflow cooling and 2) rain incursion into the updraft. First, the maximum θ_v deficit in the inflow region at 0051 UTC (during the peak of the merger) was up to 4°C colder than θ_v deficits measured in this region at 0012 UTC (prior to the merger) (Fig. 5), and equivalent potential temperature deficits were up to 2°C colder (not shown). Second, as cell A approached and then merged with the nontornadic supercell, the supercell updraft became increasingly ensconced in reflectivity (not shown). Quantitatively, the percentage of points in the updraft ($w > 10$ m s^{-1} at 2.1 km) having reflectivity values exceeding 35 dBZ jumped from a little above 10% to around 85% between 0024 and 0033 UTC. As the mesocyclone and updraft weakened, likely for the aforementioned reasons, the nontornadic storm increasingly lost its supercellular structure and was ultimately consumed by cell A. This evolution is consistent with the model presented by Hastings and Richardson (2016) for a merger between a younger cell and a supercell that leads to the demise of the supercell due to ingestion of cold air from the younger cell's outflow.

During this time, outflow from cell A was also interacting with the northern flank of the tornadic supercell and continued to do so leading up to the time of tornadogenesis (Fig. 3). These interactions may have favorably influenced baroclinicity and/or convergence in the tornadic supercell. In addition, around 0051 UTC, approximately 18 min prior to tornado formation, cell C may have merged into the rear flank of the tornadic supercell

(the uncertainty is due to insufficient temporal resolution of the WSR-88D data; none of the mobile radars captured cell C, as they were repositioning during this time) (Fig. 3a). If it did merge into the rear flank, it is not clear from the WSR-88D data if this facilitated tornadogenesis or was merely coincidental, but mergers into the rear flank have been found in simulations (Hastings and Richardson 2016) to amplify low-level rotation. Observational studies have suggested a link between tornado events and rear-flank mergers as well (Rogers and Weiss 2008; Rogers 2012). Finally, just prior to tornadogenesis, another small new cell (cell B), that had formed to the south, merged into the far forward flank of the tornadic supercell (Figs. 1d–g). Numerical simulations by Hastings and Richardson (2016) predict a multicore system for updrafts interacting in this manner. In the present case, however, the new cell merged with the mass of precipitation to the north from the previous mergers, rather than remaining a separate entity.

Several interactions between the supercells and smaller cells occurred in this case. In particular, cell interactions limited the ability of the nontornadic cell to remain supercellular for as long as the tornadic supercell. The influence of cell interactions on the tornadic supercell is less clear, given available observational data. We now compare their environments for further clues about why one supercell produced tornadoes and the other did not.

4. Storm environments

Given the relationship between environmental characteristics and the likelihood for tornado formation, as
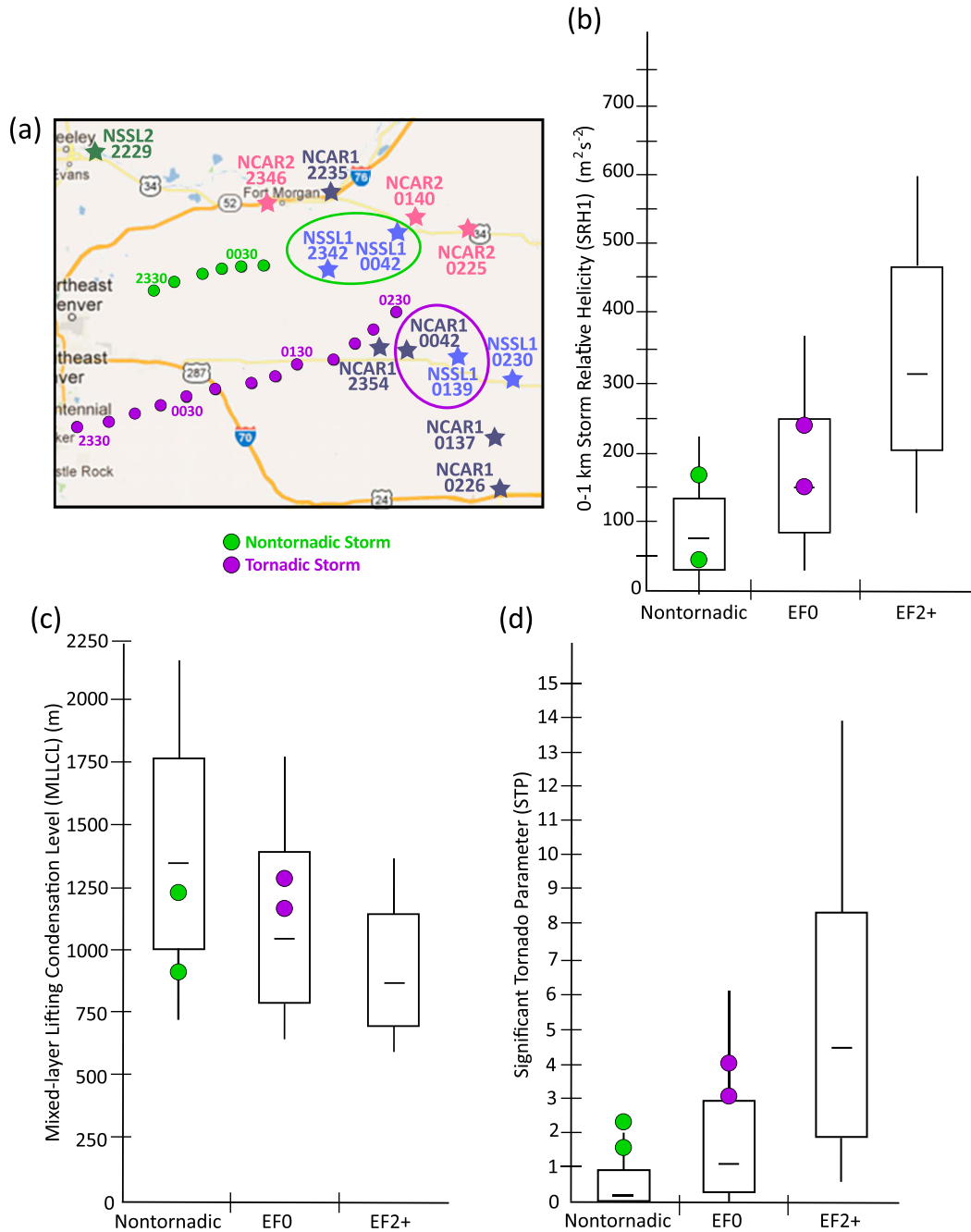
FIG. 6. (a) Map showing the soundings used to define the environmental conditions of the nontornadic and tornadic storms. The colored dots show the midlevel mesocyclone locations for the nontornadic supercell (bright green) and tornadic supercell (purple), every 15 min. The bright green (purple) circuit denotes the soundings most representative of the storm environment of the nontornadic (tornadic) supercell, based on temporal and spatial proximity. (b)–(d) Adapted from Thompson et al. (2012). Box-and-whisker plots of climatology of nontornadic, EF0 (weakly tornadic), and EF2+ (significantly tornadic) storm environments for discrete right-moving supercells represented by (b) 0–1-km storm-relative helicity, (c) mixed-layer lifting condensation level, and (d) significant tornado parameter overlaid with the ranges from 10 Jun 2010. Green dots show the values of the given parameter in the environment of the nontornadic supercell, and purple dots show the values in the environment of the tornadic supercell.
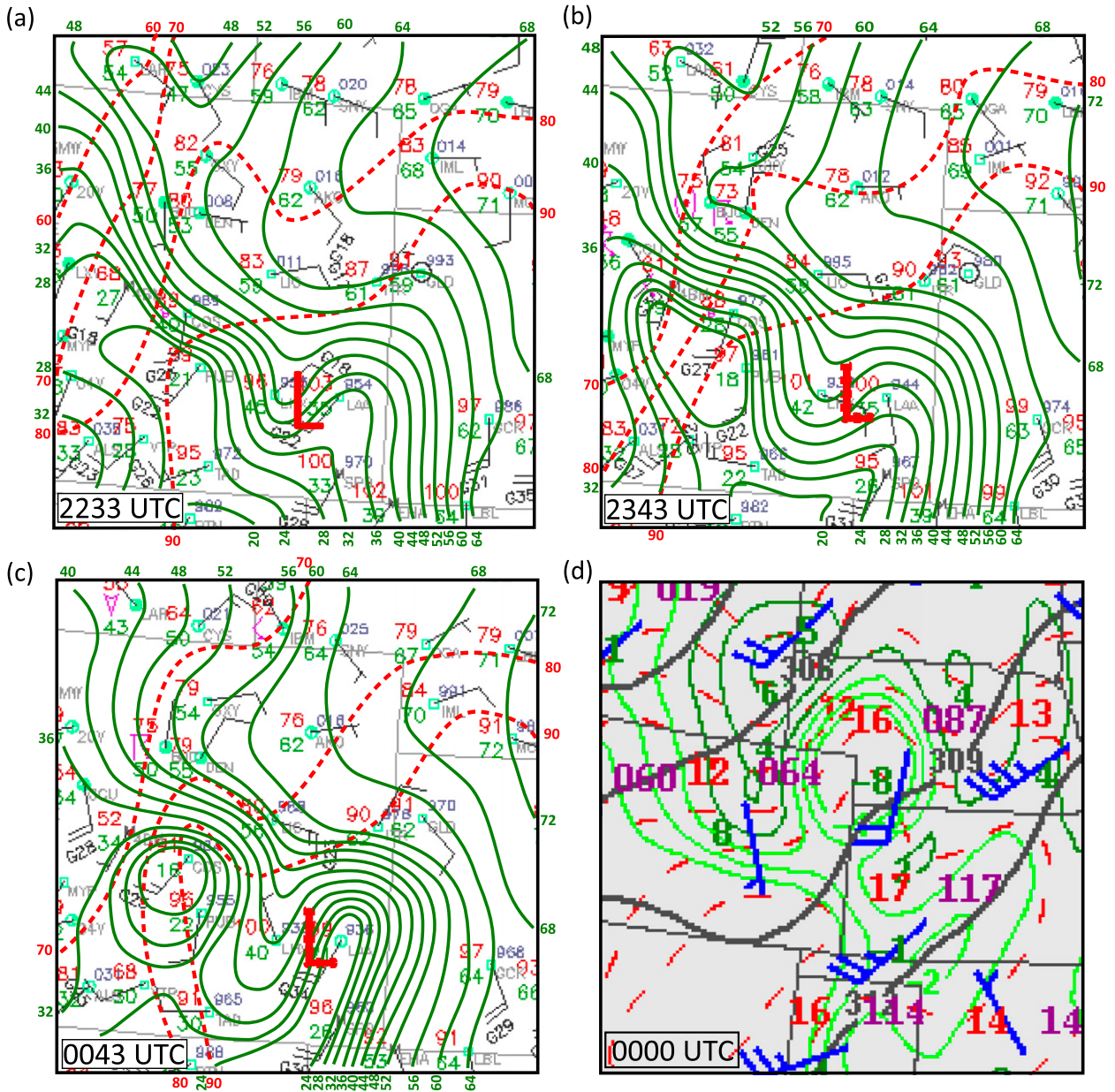
FIG. 7. (a)–(c) Global Telecommunications System (GTS) surface station plots from 10 Jun at 2233, 2343, and 0043 UTC (11 Jun), courtesy of NOAA. Times were chosen to be as close as possible to those of the mobile soundings. Station models show the temperature, dewpoint temperature (both in °F), wind speed and direction, and cloud cover at particular locations. Green and red (dashed) lines are subjectively analyzed isodrosotherms and isotherms, respectively. Here "L" indicates the low pressure center in southeast Colorado. (d) Mesoanalysis from the Storm Prediction Center at 700 hPa. Station plot shows temperature, dewpoint temperature (both in °C), pressure, and wind speed and direction. Red, dashed lines are isotherms. Green lines are isodrosotherms for dewpoint temperatures greater than −4°C.

discussed in the introduction, we next examine the environment. A total of 13 soundings were launched in the environment ahead of the storms from 2235 to 0230 UTC (Fig. 6a). Of these, the four (two for each storm) soundings closest in space and time to the two storms are used to characterize the near-storm environmental characteristics of each (Fig. 6a). When two soundings were a

similar distance from the storm, we chose the one more likely to represent properties of air entering the storm at low levels based on the storm-relative wind directions. For example, we use the (NSSL1) 2342 UTC sounding rather than the (NCAR2) 2346 UTC sounding for the nontornadic storm, and we use the (NSSL1) 0138 UTC sounding rather than the (NCAR1) 0137 UTC
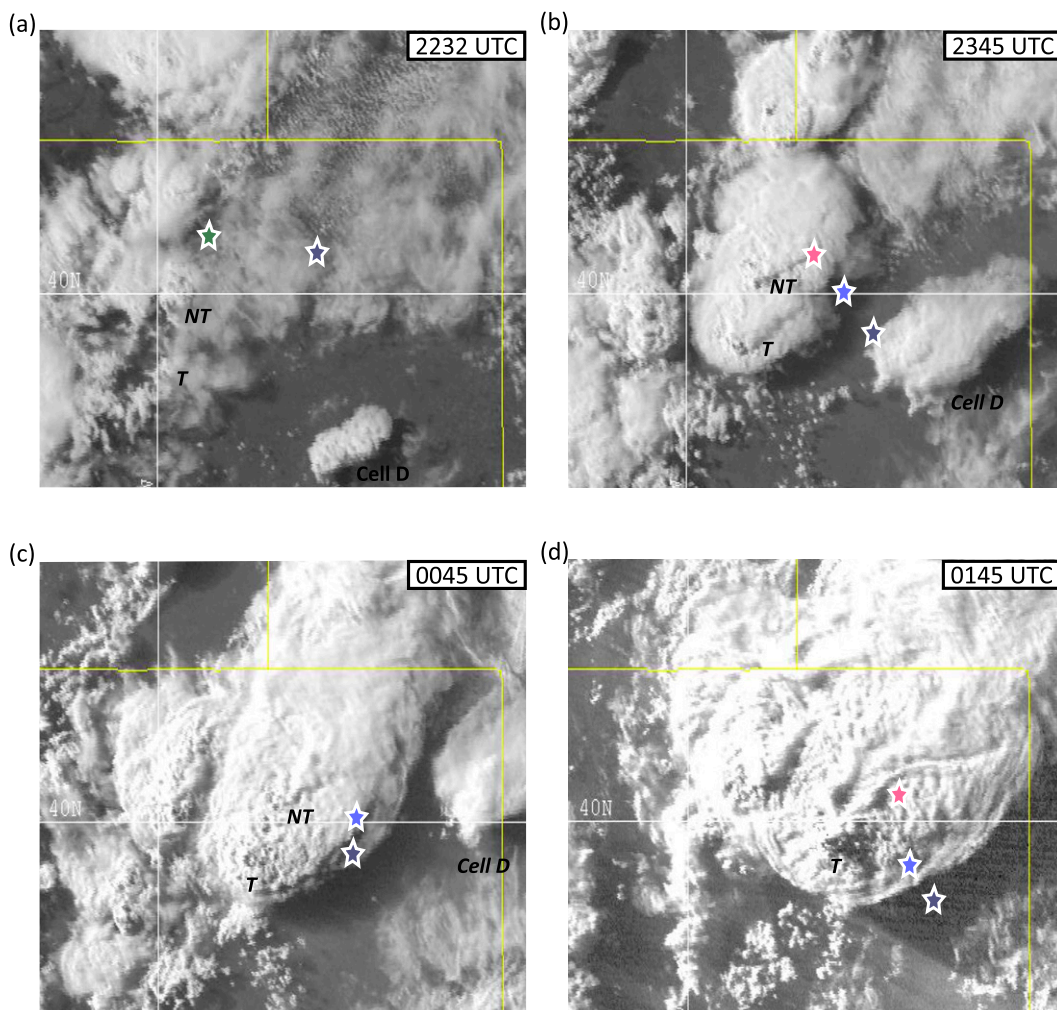
FIG. 8. Visible satellite images from *GOES-13* at (a) 2232, (b) 2345, (c) 0045, and (d) 0145 UTC. Stars correspond to sounding locations shown in Figs. 9–13. Cells of interest are labeled in each image.

sounding for the tornadic storm. For the nontornadic supercell, we focus on the time period during which it was mature until just after its interaction with cell A (2342–0042 UTC). For the tornadic supercell, we cover the time period within 30 min on either side of the tornadic phase[2] (0042–0138 UTC).

In general, the tornadic storm environment fits the climatology for a weakly tornadic storm, while the nontornadic storm environment fits better with the nontornadic storm climatology based on Thompson et al. (2012). To better understand the spatial and temporal variations leading to these differences, we first examine the individual soundings as well as surface and 700-hPa analyses.

On 10 June 2010, the northeastern corner of Colorado resided in an environment containing both thermal and moisture gradients (Fig. 7). A dryline was evident near the Colorado–Kansas border and was associated with a low pressure center in southeastern Colorado, with easterly low-level flow in northeastern Colorado that advected higher dewpoints into the region from Kansas and southwestern Nebraska (Figs. 7a–c). The result was a complex moisture distribution, with a fairly steady moist axis running from Imperial, Nebraska (IML), to Akron, Colorado (AKO). Dewpoints over 50°F were confined to north of the Palmer Divide, with a strong moisture gradient south of Limon, Colorado (LIC). This surface temperature and moisture pattern will be evident in the environmental soundings discussed below. The pattern was similar at 700 hPa (Fig. 7d), with mesoanalyses from the Storm Prediction Center (Bothwell et al. 2002) indicating a strong moisture gradient in a similar location south of LIC.

---

[2] The grouping we chose to characterize the nontornadic and tornadic supercells is different than that used by Parker (2014) for this case, owing to our stricter spatial and temporal criteria.
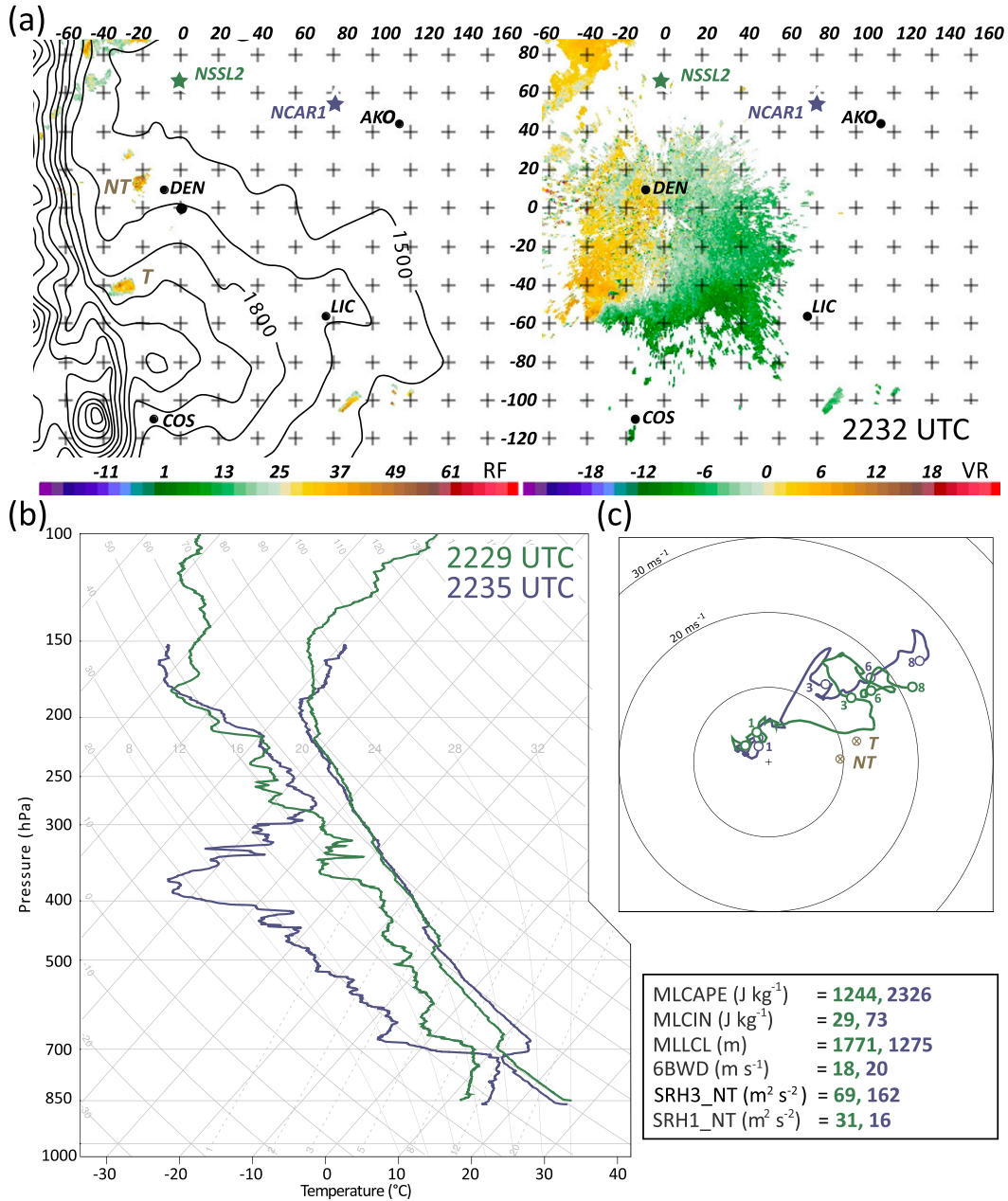
FIG. 9. (a) (left) Z_e (dBZ) and (right) radial velocity (m s^{-1}) from the KFTG radar at 2232 UTC. Reflectivities below 15 dBZ have been removed for clarity. Approximate terrain contours are overlaid for elevations above 1500 m. The green and dark blue stars correspond to the locations of the NSSL2 and NCAR1 soundings at 2229 and 2235 UTC, respectively; NT denotes the northern, nontornadic storm while T denotes the tornadic storm. Tick marks indicate distance from the KFTG radar in km. (b) Skew T–log$p$ diagram of soundings shown in (a). (c) Hodographs obtained from the same soundings. Numbers along the hodograph trace denote heights (km AGL), and the unlabeled circle denotes a height of 500 m. Labeled cross-hatched circles denote the storm motion of the tornadic and non-tornadic supercells. Relevant environmental properties are indicated in the chart at the bottom right. SRH1_NT and SRH3_NT refer to SRH1 and SRH3 computed using the motion of the nontornadic supercell.

The synoptic-scale features on 10 June, combined with the terrain, generated a favorable environment for the development of severe weather near Denver, Colorado. At 2232 UTC, the two eventual supercells of interest were visible in satellite imagery (Fig. 8a) and as small echoes on radar (Fig. 9a) approximately 50 km apart along a north–south line. The southern cell (which later became tornadic) formed near the intersection of the Palmer Divide and the
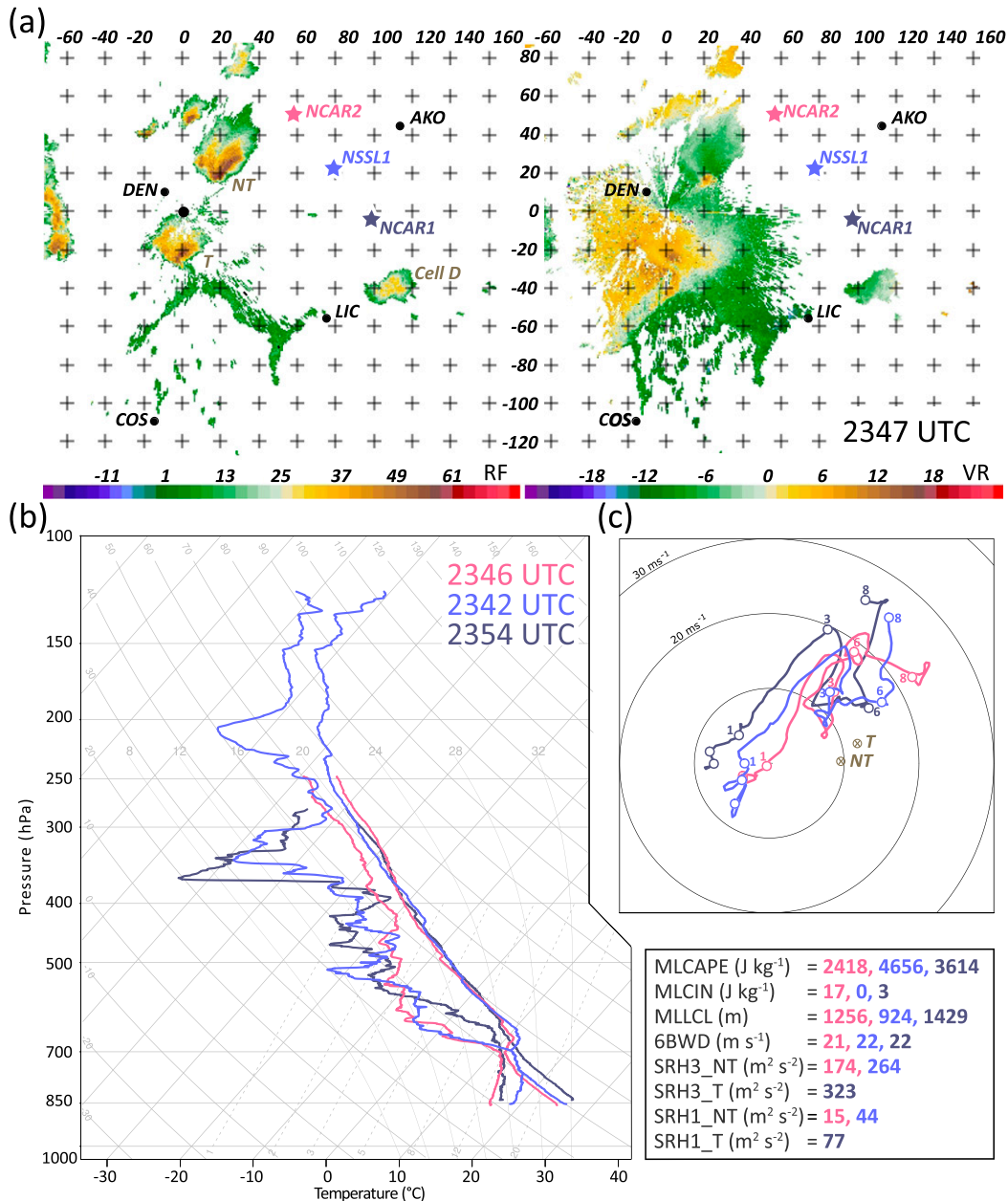
FIG. 10. As in Fig. 9, but at 2347 UTC, and reflectivities below 2 dBZ have been removed for clarity. The pink, bright blue, and dark blue colors correspond to the NCAR2, NSSL1, and NCAR1 soundings at 2346, 2342, and 2354 UTC, respectively. The two unlabeled circles denote heights of 250 and 500 m. SRH1_T and SRH3_T refer to SRH1 and SRH3 computed using the motion of the tornadic supercell.

Rockies. Another cell (hereafter, cell D) formed slightly earlier on the southeast side of the Palmer Divide ($x = 100$ km, $y = -100$ km in Fig. 9a). Cell D did not appear to interact directly with the two supercells of interest, but it did move to the north quickly ahead of them, likely modifying the environment as discussed below.

Two soundings were taken around 2230 UTC at locations shown in Fig. 9a. These soundings, which are north of the eventual storm tracks, confirm the basic pattern of boundary layer moisture increasing from west to east across that part of the domain, with a small temperature contrast at the surface, in agreement with the surface analysis. Deep-layer shear (6BWD) was sufficient for supercells (i.e., >18 m s^{-1}), but SRH1 and 0–1-km shear were both well below typical values for significantly tornadic storms, while LCLs were higher than those associated
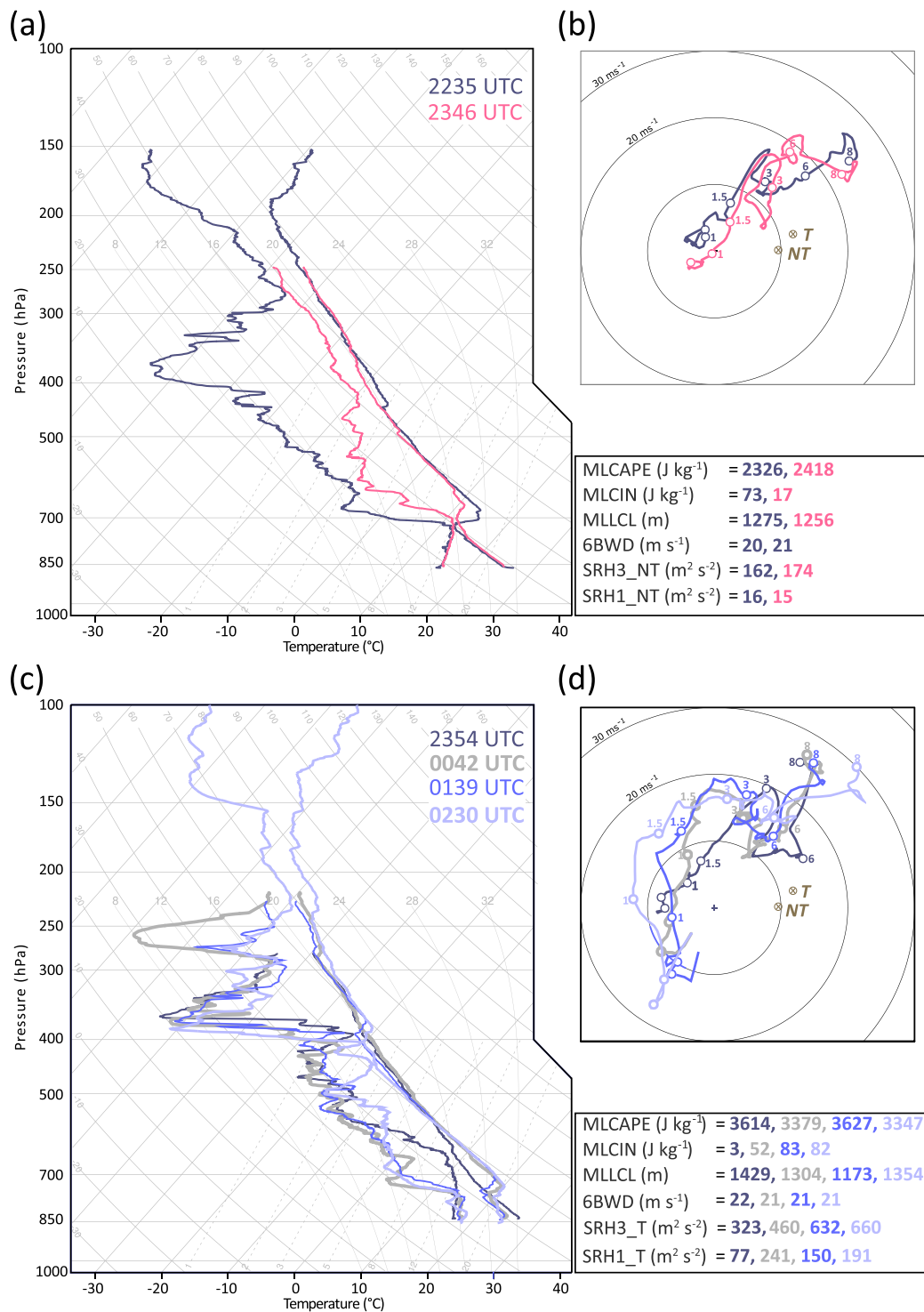
FIG. 11. Skew T–logp diagrams and hodographs showing the temporal evolution from (a),(b) 2235–2346 UTC for the NCAR1 (dark blue) and NCAR2 (pink) soundings and (c),(d) 2354–0230 UTC for the NCAR1 (dark blue and gray) and NSSL1 (bright blue and pale blue) soundings. Soundings are taken at similar locations within each panel.
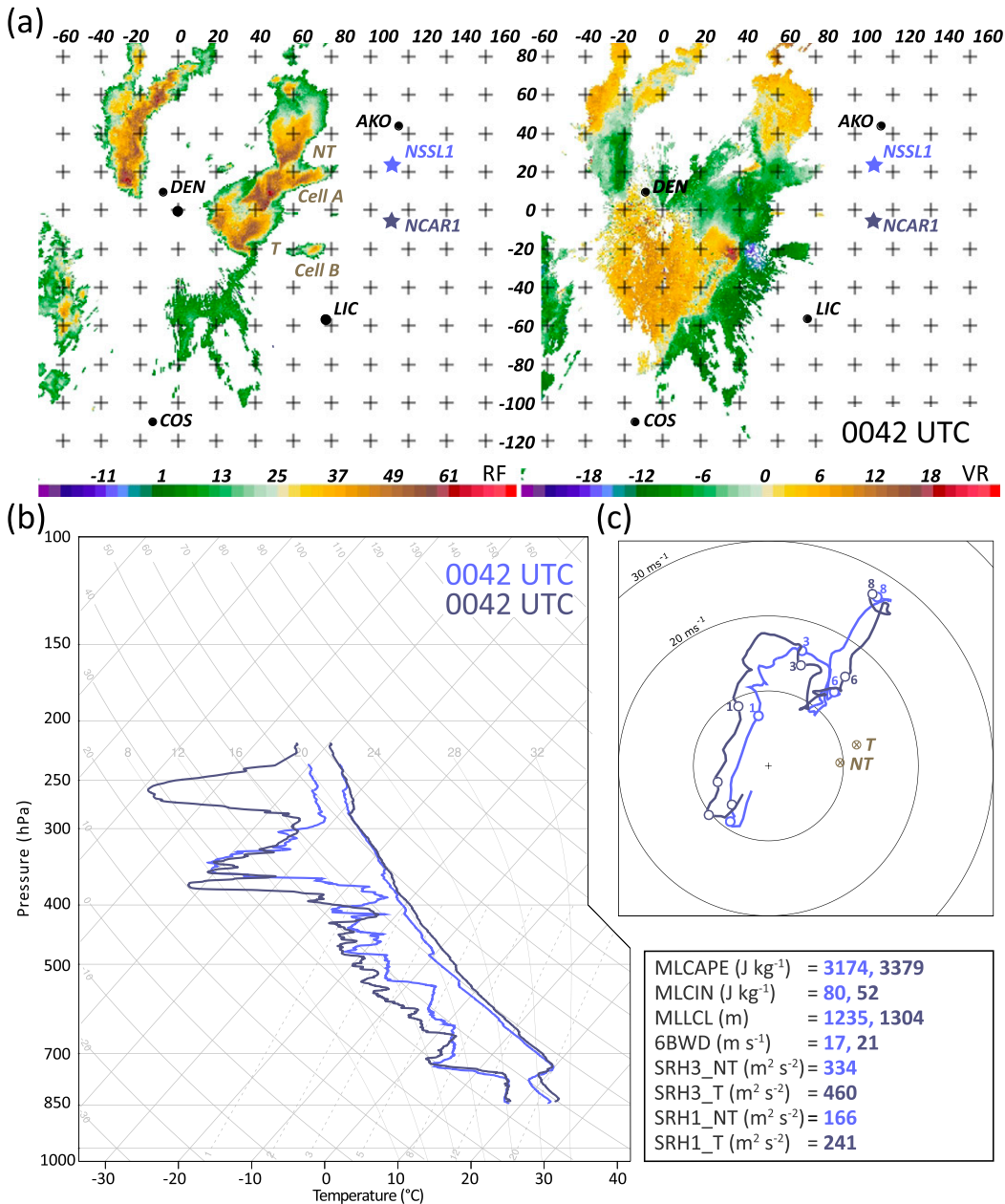
FIG. 12. As in Fig. 10, but at 0042 UTC. The bright blue and dark blue colors correspond to the NSSL1 and NCAR1 soundings, respectively, at 0042 UTC.

with significantly tornadic storms (Thompson et al. 2003, 2012) (values for these parameters are listed in Fig. 9 and the climatological values are shown in Figs. 6b and 6c).

By 2347 UTC, the two storms of interest were well-developed supercells (Fig. 10a). Three soundings taken ahead of the storms in a northwest–southeast line at about this time indicate very small values of CIN ($<20\,\mathrm{J\,kg^{-1}}$) and MLCAPE between ~2400 and $4650\,\mathrm{J\,kg^{-1}}$ (values are given in Fig. 10). CAPE is largest and LCL is lowest for the middle sounding, which was

taken near the low-level moist axis extending into Colorado from Nebraska (Fig. 7b). All of the soundings are consistent with deep boundary layer mixing (e.g., potential temperature and water vapor are nearly constant with height in the layer next to the surface). The southernmost sounding shows the deepest mixed layer and the warmest boundary layer temperatures, consistent with both the analyzed temperature field in the region (cf. Fig. 7b) and the fact that its location was relatively cloud free, while the two northernmost soundings were in a region of either
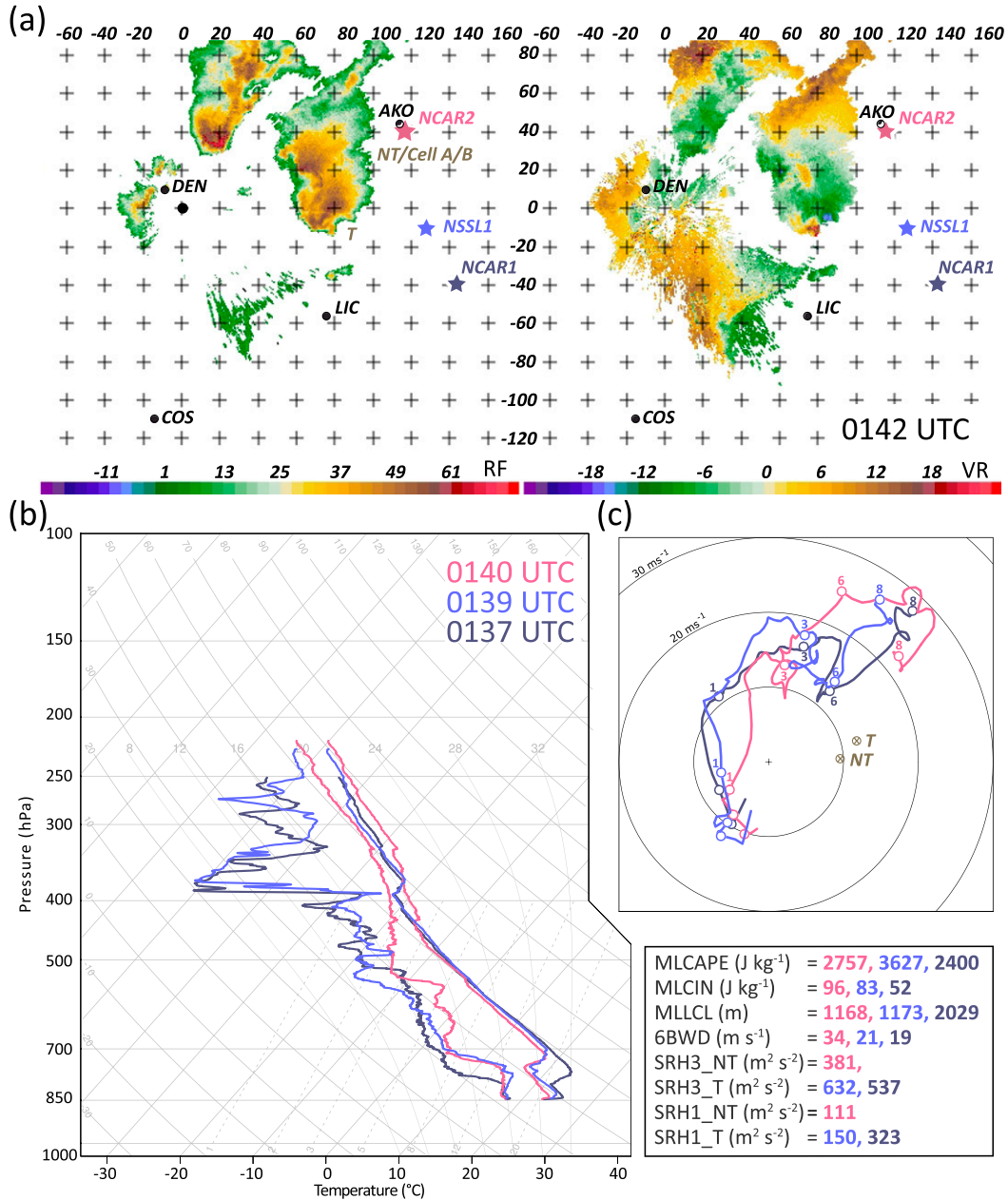
FIG. 13. As in Fig. 10, but at 0142 UTC. The pink, bright blue, and dark blue colors correspond to the NCAR2, NSSL1, and NCAR1 soundings at 0140, 0139, and 0137 UTC, respectively.

thick anvil (pink star; note the nearly saturated layer aloft) or anvil shading (bright blue star) (Fig. 8b). Relatively strong (10–20 m s^{-1}) southerly to south-southeasterly winds in the 1.5–3-km AGL layer likely resulted in trajectories that brought storm-modified air (from cell D) into the region between 700 and 600 hPa. Indeed, dewpoint values at all three of these locations at 700 hPa are anomalously high (10°–12°C) compared to any others at 0000 UTC (Fig. 7b) in the surrounding regions. The degree to which these soundings are modified by the

nearby storms cannot be assessed quantitatively given the available data, but the profiles suggest a combination of vigorous boundary layer mixing and storm modification is likely keeping dewpoints high up to at least 700 hPa. Comparing the northern sounding to one taken at a nearby location at 2235 UTC (Fig. 11a), changes are consistent with a deepening mixed layer and the incursion of the northern supercell's anvil into this region. Almost no change is evident throughout most of the boundary layer.
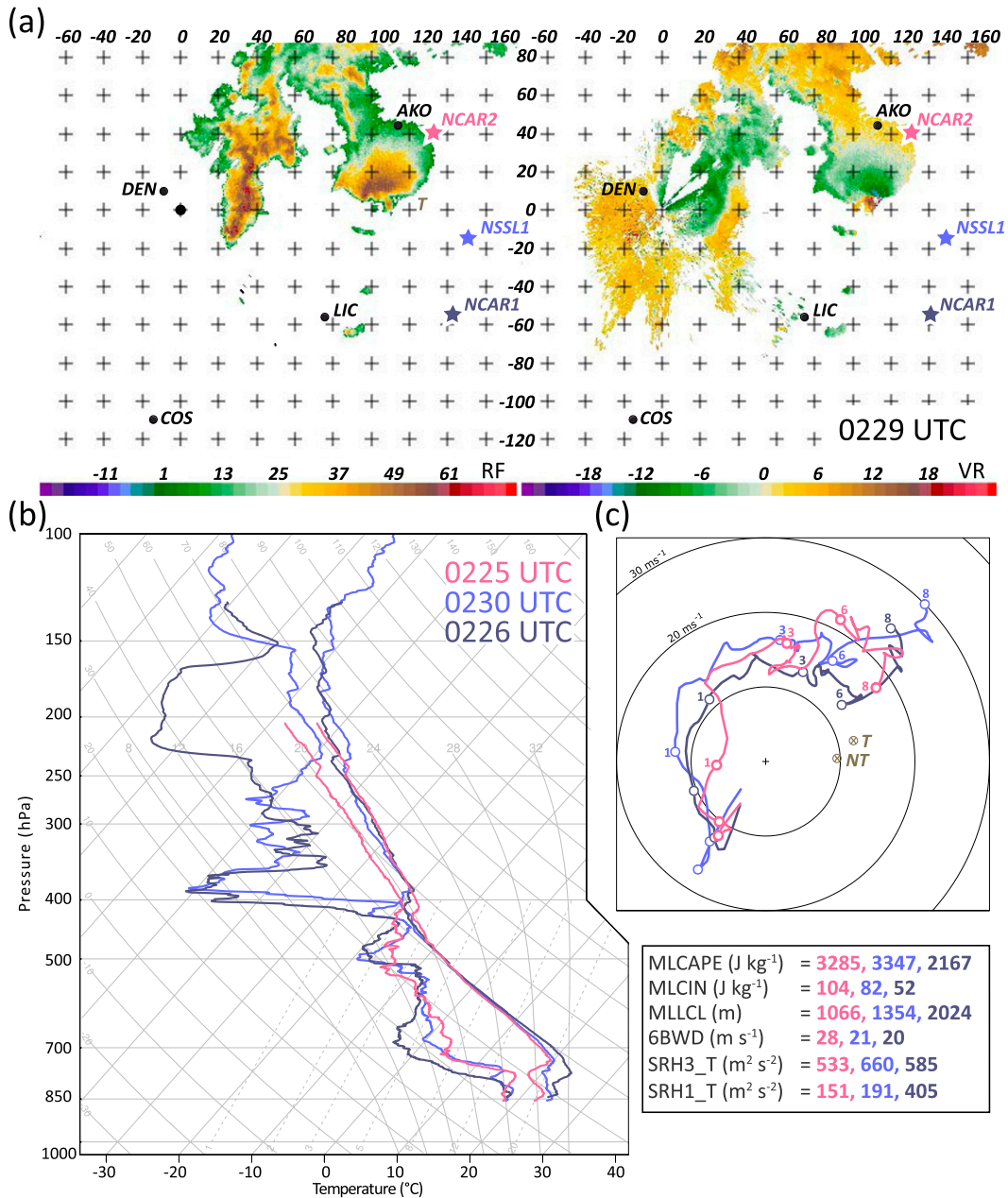
FIG. 14. As in Fig. 10, but at 0229 UTC. The pink, bright blue, and dark blue colors correspond to the NCAR2, NSSL1, and NCAR1 soundings at 0225, 0230, and 0226 UTC, respectively.

The wind profiles at ~2345 UTC (Fig. 10c) show 6BWD adequate for supercells, with SRH1 below the cutoff typically associated with significant tornadoes (i.e., $<100 \, \text{m}^2 \, \text{s}^{-2}$). SRH1 is largest for the southernmost sounding, which is nearer the tornadic storm, largely owing to greater storm-relative wind speeds. Thus, while all of the soundings support severe, deep convection, the northern two are marginal for even weak tornadoes based on SRH1 (Figs. 6b and 10; Thompson et al. 2012).

Both storms of interest progressed eastward over the next hour, and soundings taken around 0042 UTC (Fig. 12b) show a substantial change in the environment ahead of the storms, particularly in the 750–600-hPa (~1–3 km AGL) layer, which warmed and dried, lowering the depth of the mixed layer. This change is evident when comparing the southern sounding to one taken within ~10 km at 2354 UTC (Fig. 11c). Winds in the 1–3-km layer increased in speed (Fig. 11d) and were oriented approximately opposite and along the gradients of
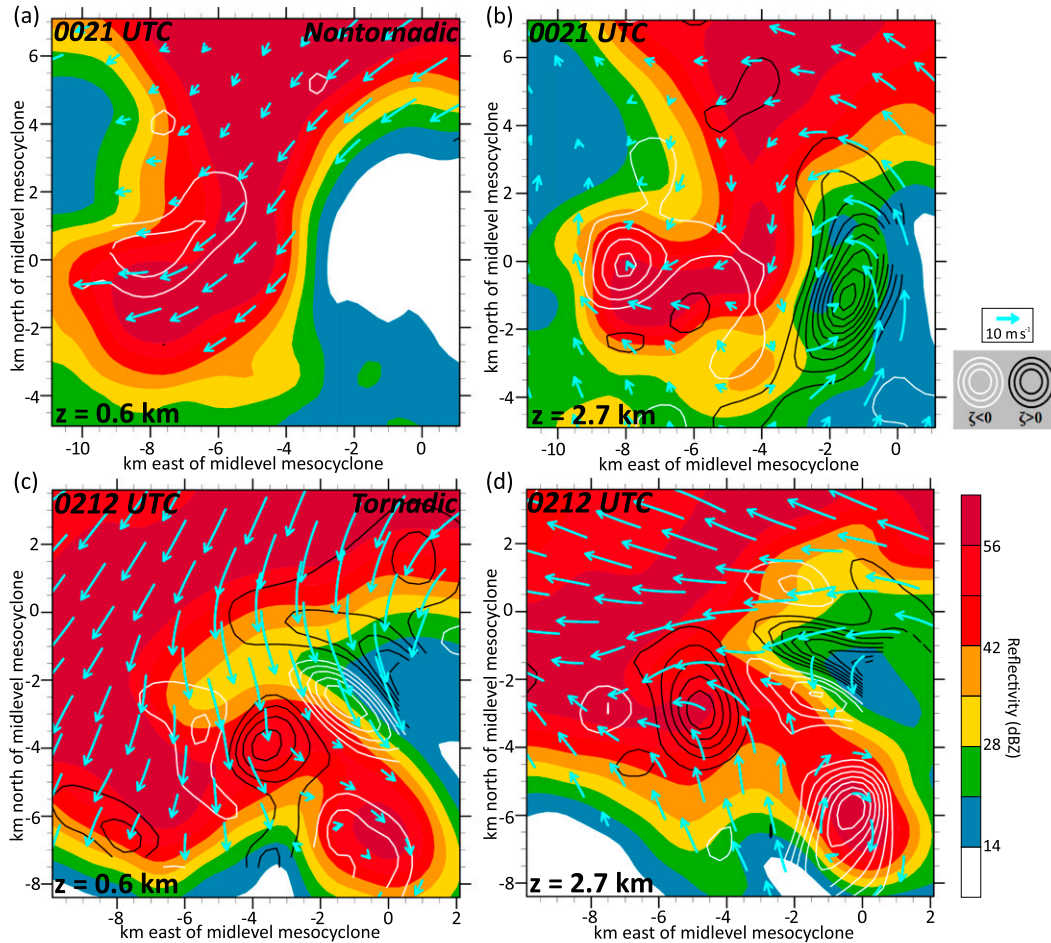
FIG. 15. Dual-Doppler-derived, horizontal, storm-relative winds (blue vectors) and vertical vorticity (contoured every $4 \times 10^{-3}\,s^{-1}$, positive in black, negative in white, with the zero contour omitted) overlaid on objectively analyzed SR2 Z_e (shaded, dBZ) of the nontornadic supercell at 0021 UTC at (a) 0.6 and (b) 2.7 km and the tornadic supercell at 0212 UTC at (c) 0.6 and (d) 2.7 km. Note that the wind data have 300-m resolution, but only a small percentage of the vectors are plotted here for the sake of clarity.

temperature and moisture, respectively, at 700 hPa (Fig. 7d). Thus, magnitudes of advection of both temperature and moisture were also enhanced, likely leading to some of the warming and drying in this layer, which also may have been in a region of descent on the periphery of the convection. Cell D had moved off to the northeast (Fig. 8c) and was no longer providing this region with moist, storm-modified air. Thus, properties returned to profiles closer to those observed at 2235 UTC (Fig. 9b), except for greater moisture aloft in the layer of strong southwesterly winds (Fig. 12b). Quantifying the relative contributions of these processes is impossible given the paucity of upper-level data south of the soundings.

Coincident with these large thermodynamic changes were significant changes in the hodographs below 3 km (Figs. 12c and 11d), likely related to a sharp decrease in mixing in this layer as the environment stabilized.

Mixing may have been further affected by cooling under the anvil as shown by Frame and Markowski (2013). A shortwave trough at 700 hPa also was entering the region (Fig. 7d) and likely affecting the wind profiles. These wind profile changes are similar to those documented during the early evening transition by Coffer and Parker (2015). SRH3 increased by 42%, while SRH1 tripled near the tornadic storm between 2354 and 0042 UTC (Fig. 11c), suggesting an environment much more supportive of tornado formation.

Although the 2354 UTC sounding is slightly warmer near the surface than the later soundings (Fig. 11c), little else is different thermodynamically below 750 hPa or above about 600 hPa, despite the drastic changes between these levels (Fig. 11c). The thermodynamic environment at the locations in this temporal series changed little after 0042 UTC, while the hodographs continued to
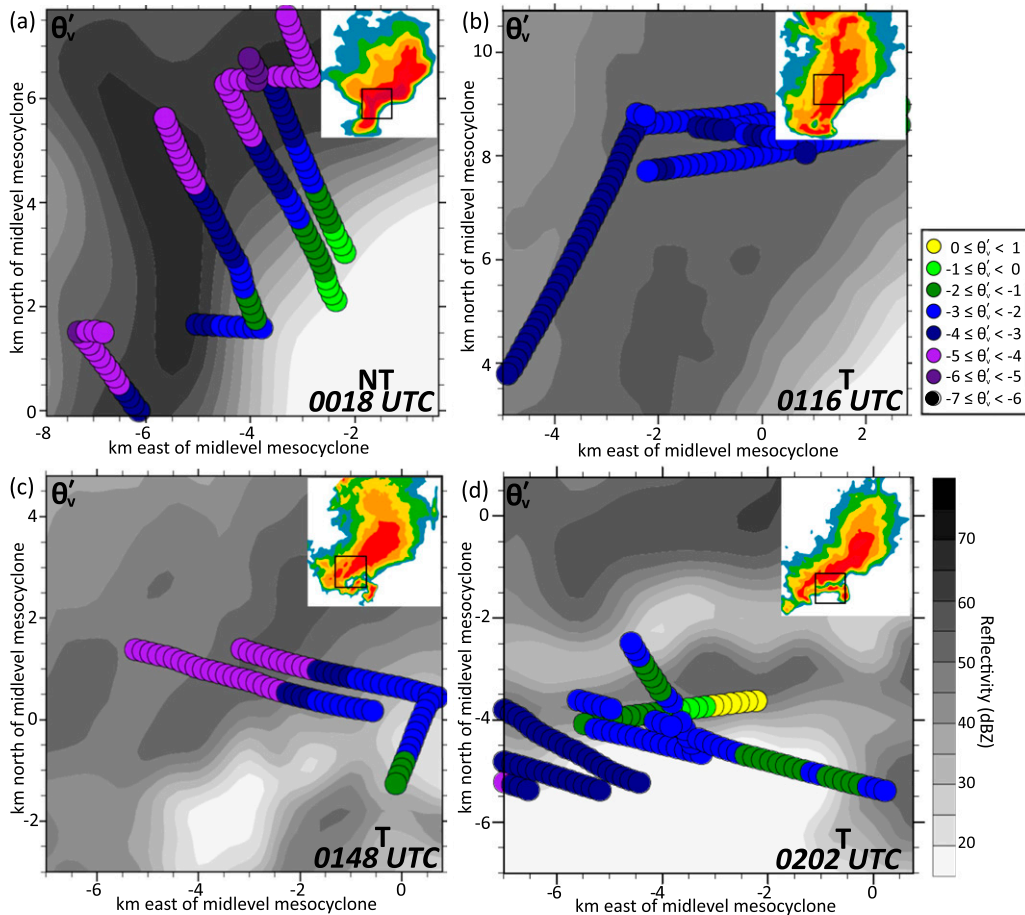
FIG. 16. Mobile mesonet–measured virtual potential temperature perturbations (color-coded circles) in the outflow of (a) the nontornadic supercell at 0018 UTC (base state: 315.9 K), (b) the tornadic supercell at 0116 UTC (base state: 314.7 K), (c) the tornadic supercell at 0148 UTC (base state: 314.7 K), and (d) the tornadic supercell at 0202 UTC (base state: 314.7 K). Temperature perturbations are overlaid on objectively analyzed Z_e from SR2 (750 m), DOW7 (800 m), NOXP (800 m), and NOXP (750 m), respectively. In the inset at the top right of each plot, the domain of each plot is denoted (black box) relative to the storm as a whole. [Note that the deficits of 1°C and less (the yellow and bright green dots) in (d) are eliminated when using a shorter steady-state assumption, thus making the data more self-consistent; the lack of consistency with the data presented here may be due to fast temporal evolution of the storm at this time, and/or an unrepresentative advection correction for this particular time/location.]

evolve, with winds at 1 km changing from southeasterly at 0042 UTC to easterly thereafter (Fig. 11d). Overall, SRH1 in this series is a maximum at 0042 UTC but still supportive of at least weak tornadoes (i.e., >100 m²s⁻²) for the rest of the VORTEX2 deployment. Spatially, SRH1 at 0142 (Fig. 13) and 0230 UTC (Fig. 14) continued to show a gradient toward the south, while the middle sounding had the greatest CAPE and SRH3.

To summarize thus far, the environment in which the supercells developed and evolved varied both spatially and temporally. Even early in the storms' evolution, there was slightly greater low-level storm-relative helicity in the environment of the tornadic supercell. Both 0–1- and 0–3-km storm-relative helicity increased significantly as the storms continued to evolve, along with a

strengthening of the storm-relative winds and a reduction of the mixed-layer depth. Over time, the environment became more favorable for tornado production. Although the two supercells were in close proximity, there were differences in their environments over their lifetimes, partially owing to spatial heterogeneity and partially owing to temporal evolution.

All values of 6BWD (17 and 22 m s⁻¹ for the NT storm; 21 m s⁻¹ for the T storm) used for the storm environments are within the lower half of climatological values for weakly tornadic (i.e., those producing only EF0 tornadoes) discrete, right-moving supercells (hereafter referred to simply as supercells) and below the 25th percentile for supercells producing EF2+ tornadoes (Thompson et al. 2012). The small range of values is consistent with similar
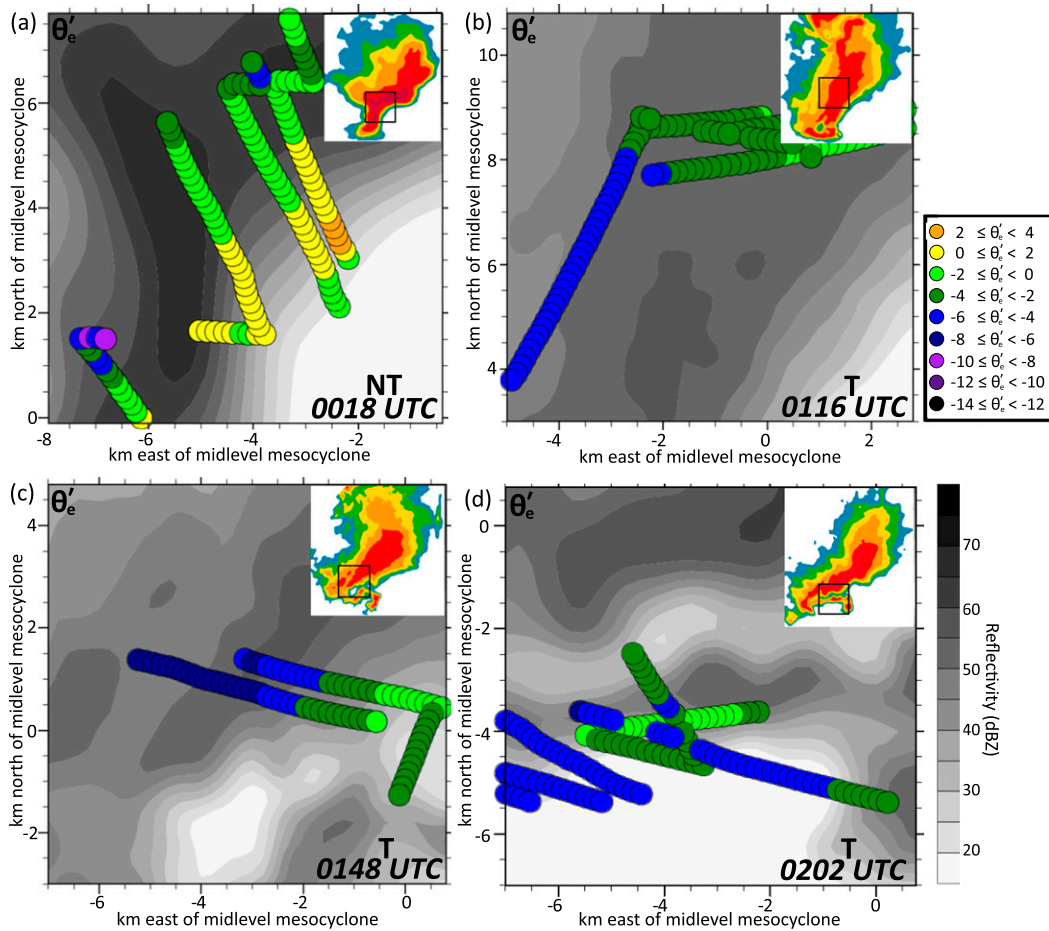
FIG. 17. As in Fig. 16, but for equivalent potential temperature, relative to a base state of (a) 356.8 and (b)–(d) 358.9 K.

gross storm characteristics for the two supercells. Values of MLCAPE (3174 and 4656 J kg^{-1} for the NT storm; 3379 and 3627 J kg^{-1} for the T storm) fall well above the 75th percentile of climatological values for all tornadic supercells (Thompson et al. 2012). MLCAPE is spatially variable (Figs. 10, 12, and 13), with the largest value occurring at 2342 UTC within the moist axis east of the nontornadic supercell. This high CAPE was short lived, returning to values below 3500 J kg^{-1} within an hour. Neither 6BWD nor MLCAPE discriminate well between the tornadic and nontornadic environments, as expected given that these parameters are more related to isolated storm type than to tornadic potential within the supercell type.

The LCL, traditionally found to be lower in tornadic supercell environments (e.g., Thompson et al. 2012), is actually a bit lower in the environment of the *nontornadic* supercell (924 and 1235 m) than in that of the tornadic supercell (1173 and 1304 m) (Fig. 6c). We note that the 924-m value was observed in only one sounding location at one time; the rest of the LCL values in both environments fit best with the distribution for weakly tornadic or

nontornadic storms (Fig. 6c) and are above (i.e., worse than) the 75th percentile for significantly tornadic storms. Values of SRH1 are higher in the environment of the tornadic supercell (150 and 241 m^2 s^{-2}) than in that of the nontornadic supercell (44 and 166 m^2 s^{-2}) (Fig. 6b), suggesting the environment near the tornadic supercell was more favorable for tornado generation, with both values above the median for weakly tornadic supercells. Only at the later time (0138 UTC; just after the final tornado) is SRH1 above the 25th percentile range for significantly tornadic supercells. The nontornadic supercell experienced SRH1 below the 25th percentile for weakly tornadic supercells for most of its time as an isolated cell, reaching just above the median value for weakly tornadic storms only at the final time used (0042 UTC), when it was being affected by cell A (see discussion in section 3).

Values of the STP are higher in the environment of the tornadic supercell (3.1 and 4.0) than that of the nontornadic supercell (1.6 and 2.3) (Fig. 6d), consistent with the higher values of SRH1 in the former environment. STP values near the tornadic supercell fall above the 75th
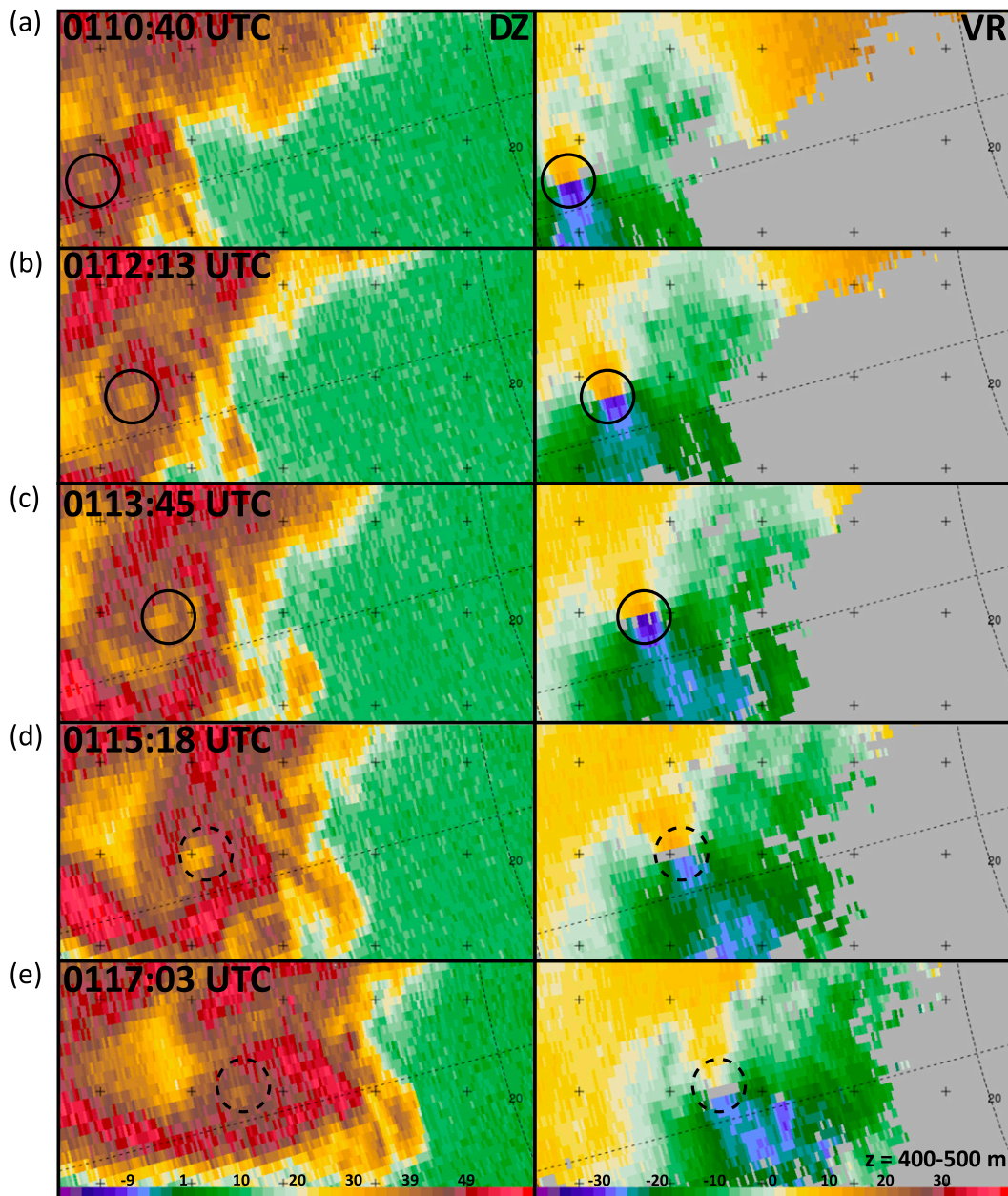
FIG. 18. Evolution of both tornadoes (and transition period in-between), shown by (left) Z_e (dBZ) and (right) velocity (m s^{-1}; removed pixels are colored gray) data at ∼ 400–500 m AGL from DOW7. Circles indicate the location of the radial velocity couplet at each time. Solid circles are used to denote times when the tornado was visible. Tick marks are spaced every 2 km. DOW7 is 30 km from the first tornado at 0110:40 UTC, and only 15 km from the second tornado at 0126:09 UTC.

percentile for weakly tornadic supercells, but below the median for significantly tornadic supercells (Fig. 6d). The STP in the nontornadic supercell environment is above the median but below the 75th percentile of climatological values for weakly tornadic supercells, and only exceeds the 25th percentile for significantly tornadic supercells near the end of its life (e.g., 0042 UTC, at which time this storm was no longer isolated) (Fig. 6d).

5. Comparison of kinematic features and outflow characteristics

We now examine the basic flow and cold pool characteristics of each supercell. Dual-Doppler analyses of the nontornadic supercell show a mesocyclone at altitudes above 2 km AGL at 0021 UTC (Fig. 15b) but a lack of strong, well-developed rotation close to the surface
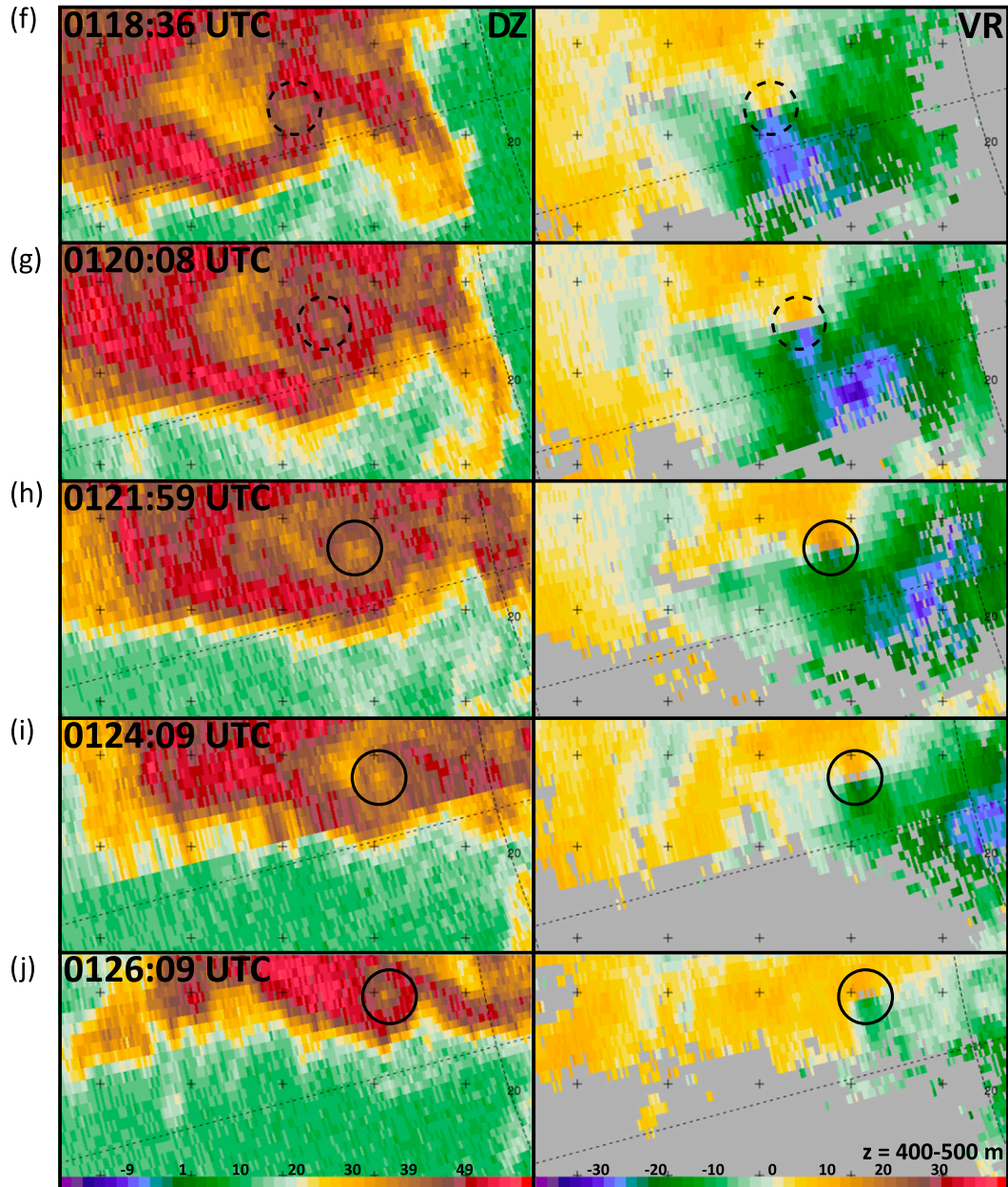
FIG. 18. (*Continued*)

(Fig. 15a). The lack of near-surface rotation may have been caused by relatively weak ($<$10 m s^{-1}) storm-relative flow through the cold pool (Fig. 15a). Parker and Dahl (2015) used an idealized heat sink to show that storm-relative flow must reach a particular magnitude (depending on the cold pool depth, flow characteristics, and likely other factors) to facilitate the production of vertical vorticity though baroclinic generation and tilting in the downdraft. Flow that was too slow in their simulations resulted in significant baroclinic production of horizontal vorticity but little tilting into the vertical within the

downdraft. It is possible that the storm-relative flow in the nontornadic storm was not sufficient for the production of significant vertical vorticity within the downdraft. The 0–1-km shear and SRH1 were also small (see section 4) over most of the nontornadic storm's time as an isolated cell, further limiting the possibility to stretch (through strong upward dynamic perturbation pressure gradient forces) any vertical vorticity that did develop. On the other hand, the tornadic supercell exhibited significant low-level rotation during the VORTEX2 deployment. For example, at 600 m, a cyclonic vorticity maximum was evident at

0212 UTC (Fig. 15c). Note the nonzero storm-relative flow through the core of this vortex, especially at 2.7 km (Fig. 15d); this flow was associated with the rearward storm-relative motion of cyclonic vortices (including this vortex) that will be elaborated upon in section 7. It should be noted that dual-Doppler coverage was not optimal at lower levels in either storm owing to somewhat large baselines or poor dual-Doppler geometry in the areas of interest, and data quality was an issue in low-reflectivity regions. However, video collected by the photogrammetry team further supports these perceived differences in low-level rotation. Their real-time notes state that "while the storm-scale features were visually impressive, little low-level rotation was observed" in the nontornadic storm. Regarding the tornadic storm, they state that "despite the presence of a well-defined and intensifying low-level mesocyclone, no other tornadoes were visually observed with the storm" after the first two tornadoes.

Regarding the cold pool, measurements collected by the mobile mesonet fleet suggest that neither storm on 10 June 2010 had particularly large virtual potential temperature (θ_v) deficits across the outflows, with maximum deficits rarely exceeding 5°–6°C. For example, at 0018 UTC, a θ_v deficit of 5°C was measured across the nontornadic supercell's RFD, which falls within the typical range of θ_v deficits in nontornadic/weakly tornadic supercells of 4°–7°C (Markowski et al. 2002) (Fig. 16a). During the tornadic supercell's nontornadic phase, at 0148 UTC, a θ_v deficit of 5°C was also observed in a similar region (Fig. 16c), followed by a θ_v deficit of 4°C (Fig. 16d) at 0202 UTC. StickNet measurements (only available for the tornadic supercell) showed deficits of up to 7°C farther west in the rear flank at 0202 UTC (not shown). During the tornadic supercell's tornadic phase, unfortunately, there were only measurements available in the northern flank of the storm owing to a sparse road network and ongoing redeployment. However, where data were available, the maximum θ_v deficit was 4°C, not much warmer than θ_v deficits in the nontornadic supercell (Fig. 16b).

Additionally, mobile mesonet measurements suggest that maximum equivalent potential temperature deficits across the outflows rarely exceeded 8°C in either storm prior to 0200 UTC (11 June). For example, at 0018 UTC in the nontornadic supercell, the maximum θ_e deficit was 6°C (Fig. 17a), much smaller than the typical θ_e deficit measured in nontornadic supercells of 10°–12°C (Markowski et al. 2002). The θ_e deficit was 6°C at 0116 UTC (Fig. 17b), 8°C at 0148 UTC (Fig. 17c), and 6°C at 0202 UTC (Fig. 17d) in the tornadic supercell. StickNet measurements showed a θ_e deficit of 12°C at 0202 UTC (not shown) farther west in the rear flank, consistent with the distribution seen in Markowski et al. (2012) and the numerical simulations of Beck and Weiss

(2013), who showed that air originating at low levels and passing through the forward-flank has much higher θ_e than air originating farther aloft and descending in the rear flank of the storm.

At most times in both storms, outflow temperatures were consistent with storms that produce weak tornadoes but also with storms that are nontornadic. Both outflows were, however, cold relative to typical outflows in significantly tornadic supercells. This highlights one of the forecasting challenges in marginal environments; storm characteristics (e.g., outflow temperature) and associated environmental parameters (e.g., LCL heights) may not be significantly different for weakly tornadic and nontornadic storms, resulting in a limited ability to forecast tornadoes.

6. Tornado evolution

We next briefly document the evolution[3] of the two (visible) tornadoes[4] produced by the tornadic supercell, as tornado production is the defining difference between the two supercells. The first tornado developed at approximately 0109 UTC (Fig. 18) and had a visually well-defined funnel (Fig. 19b), as it was located to the east of the bulk of the precipitation. It maintained a radial velocity couplet at or above tornado strength [defined here as 40 m s^{-1} following Alexander and Wurman (2008), no more than two gates apart (~500 m)], at all heights analyzed, until 0114 UTC (Fig. 19a). Then, at almost all heights, the radial velocity differential weakened by at least 5 m s^{-1}, even falling below tornado strength aloft (Fig. 19a). Correspondingly, visual ground observations indicate that the condensation funnel retracted upward from the surface a little after 0115 UTC.

For approximately the next 7 min, there was no visible condensation funnel present. During this transition time, the circulation aloft (1–2.5 km) generally maintained at least tornado strength (Fig. 19a). However, closer to the surface, around 0.5 km, the circulation had weakened by 0116 UTC, and had diminished below tornado strength

---

[3] For consistency, all of the radial velocity differential estimates use the four-field-averaged velocity (see section 2a), even though this sometimes required ignoring data in the center radial of the tornado. Inspection of individual fields containing data along the center radial (not shown) confirms the general temporal patterns of velocity differential, although exact amplitudes are slightly different.

[4] We define tornado occurrence by the presence of a visible condensation funnel associated with a strong vortex. Although a visible funnel is not necessary for a tornado to exist, on this day the visible funnels were our best indicator of the tornadic vortices. That being said, as the definition of a tornado is subjective (as is the radial velocity differential threshold we use below), we recognize the possibility that there was just one continuous tornado on 10 June.
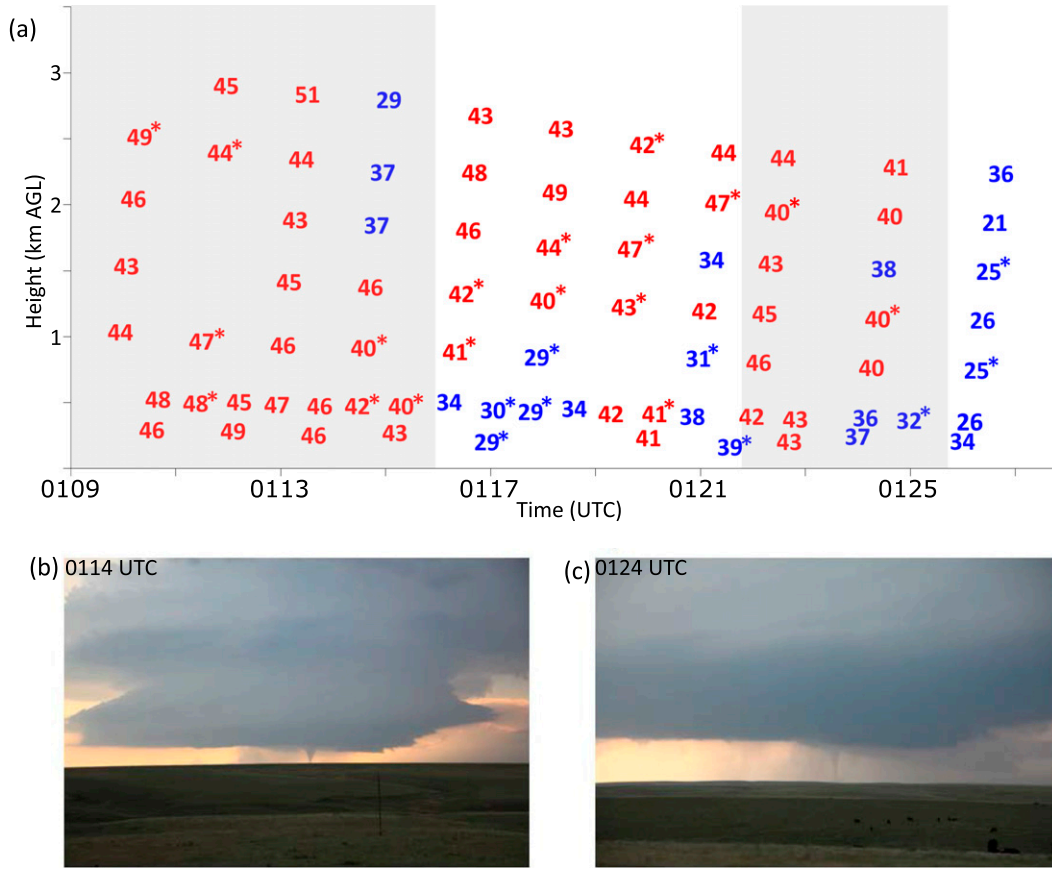
FIG. 19. (a) Radial velocity differential (m s^{-1}; red if greater than tornado threshold of 40 m s^{-1}, blue if less than 40 m s^{-1}) calculated using gate-to-gate (or one gate separation due to noise in the data; such differentials are denoted by an asterisk) radial velocity data from the raw 0.5°, 1°, 2°, 3°, 4°, 5°, and 6° DOW7 sweeps during the first tornado (0109–0115 UTC), transition period in-between (0115–0122 UTC), and the second tornado (0122–0126 UTC). Gray shading denotes the duration of the first and second tornado, respectively. (b),(c) Photographs of the (b) first tornado at 0114 UTC and (c) second tornado at 0124 UTC. Both photographs were taken by the LSC/NCAR Photogrammetry team and are looking to the west-southwest (0114 UTC) or ~west (0124 UTC).

after 0118 UTC. Even when the strength of the velocity couplet exceeded tornado strength, there was no accompanying visible funnel.

The second visible tornado began at approximately 0122 UTC (Fig. 19c). The strength of the circulation weakened at all heights throughout the tornado's short life, especially from 0124 to 0126 UTC. During these last two minutes of the visible tornado's life, the radial velocity differential was typically below tornado strength, even dipping as low as 20–25 m s^{-1} by 0126 UTC (Fig. 19a). Throughout its lifetime, the second tornado was surrounded by rain, likely due to an amplification of a surge in the rear-flank downdraft region to its south that resulted in the tornado experiencing westward motion relative to the eastward extent of high reflectivity. This surge was likely a rear-flank downdraft internal surge (e.g., Marquis et al. 2012), manifest here as eastward movement of a region of

enhanced inbound radial velocities (i.e., up to 25–29 m s^{-1}) (Figs. 18h–j), and seemed to be related to the leading edge of high reflectivity (i.e., greater than 25 dBZ). The tornado's location within the rain and relatively humid air likely aided its ability to produce a condensation funnel despite the relatively weak circulation.

The evolution of the 10 June 2010 tornadoes did not follow the classic model of cyclic mesocyclogenesis prior to the production of a new tornado (Burgess et al. 1982). Rather, the same mesocyclone that produced the first tornado generated the second tornado minutes later, similar to behavior observed by Alexander and Wurman (2005) for the Spencer, South Dakota, tornadic supercell.

7. Posttornadic kinematic evolution

As previously discussed, the tornadic supercell's mesocyclone underwent a cyclic evolution following the two
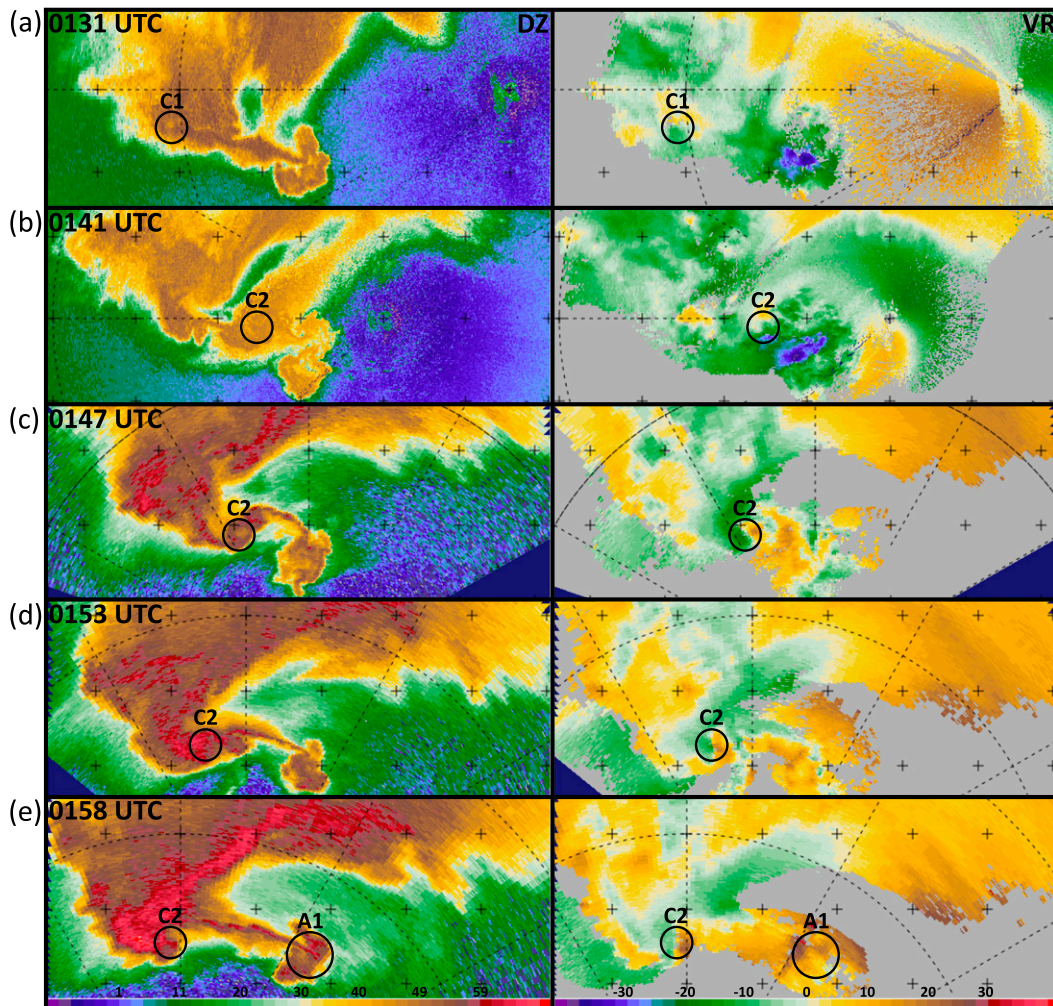
FIG. 20. (left) Z_e (dBZ) and (right) radial velocity (m s^{-1}; removed pixels are colored gray) at approximately 2–2.5 km (depending on location of particular circulation) from (a),(b) DOW7 and (c)–(j) SR2 at the times noted (approximately every 6 min). Labeled black circles denote cyclonic and anticyclonic circulations. Tick marks are spaced every 5 km. Note that DOW7 reflectivity in (a) and (b) is uncalibrated.

tornadoes. This evolution is relevant to examine, as it may help explain why the tornadic supercell underwent a long nontornadic phase. Thus, it provides further insight into what makes tornado production more or less favorable, beyond that gleaned from comparing the nontornadic and tornadic supercells. Aloft, at approximately 2–2.5 km AGL, at least two new cyclonic circulations were observed to develop in the rear-flank region of the storm and move rearward relative to the rest of the storm, consistent with the behavior of some circulations in previous studies (French et al. 2008; Dowell and Bluestein 2002a). In contrast, an anticyclonic circulation remained relatively stationary in the storm-relative framework during this time period.

Single-Doppler and limited dual-Doppler data were used to analyze the circulations, due to severe sidelobe

issues encountered by the radars collecting dual-Doppler data in low-reflectivity regions of the storm. The circulations were defined as having a diameter of 1–10 km and a radial velocity differential of at least 20 m s^{-1}, per French et al. (2008). The first cyclonic circulation identified, "C1," consisted of the remaining circulation from the second tornado. By 0131 UTC, C1 had moved backward in the rear flank (Fig. 20a) and then continued its rearward motion (relative to the motion of the storm). By 0147 UTC, the first "new" circulation ("C2") had formed in the reflectivity hook (Fig. 20b) and subsequently traveled rearward in the storm (Figs. 20c–f). During this time, an anticyclonic circulation, "A1," began significantly strengthening (e.g., Fig. 20e). Circulation A1 had been present, albeit weaker, prior to 0131 UTC. It is noteworthy that for much of the subsequent time
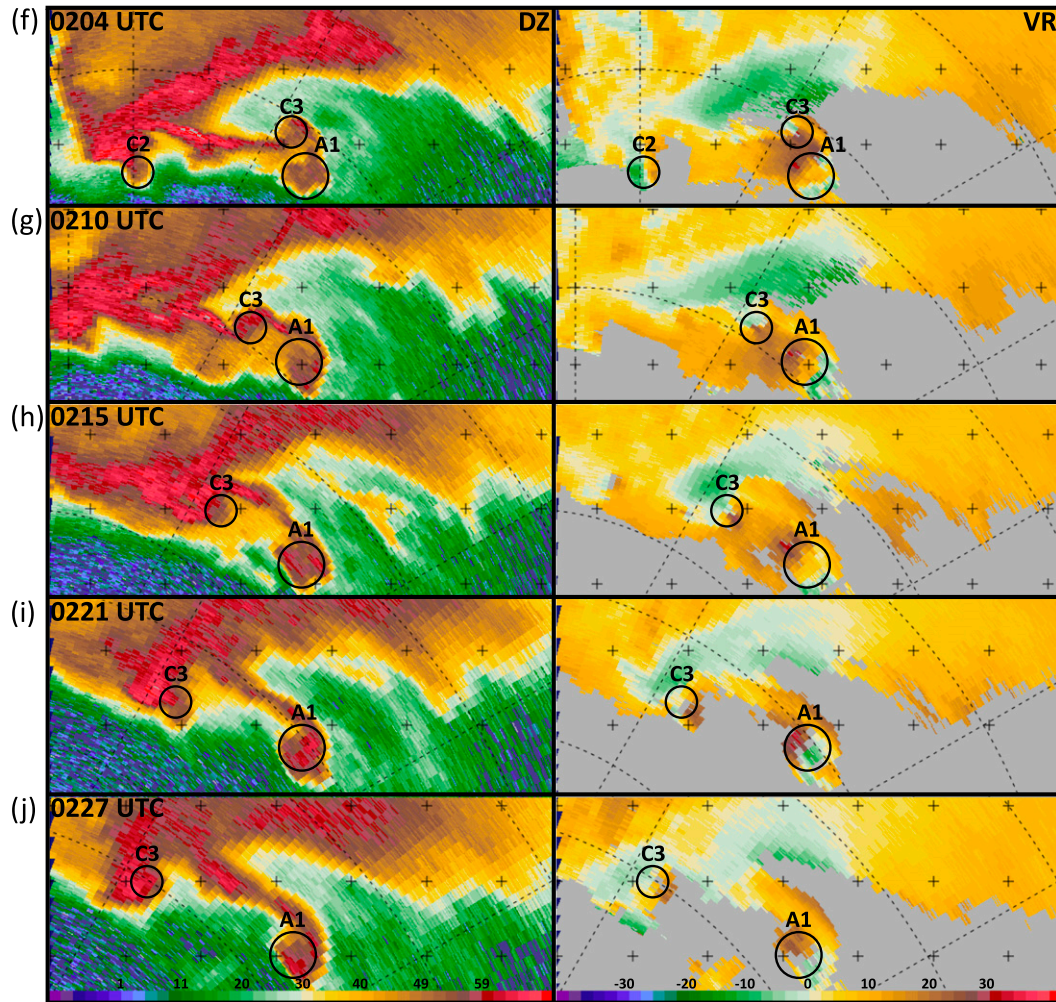
FIG. 20. (*Continued*)

analyzed, A1's strength was comparable to or greater than that of the cyclonic circulations present (based on the radial velocity differential).

By 0204 UTC, a new circulation, "C3," was rapidly developing well to the east-northeast of C2 and northwest of the anticyclonic vortex, along the rear-flank gust front (Fig. 20f). Like C1 and C2, over time, C3 moved rearward relative to the rest of the storm (Figs. 20g–j; Fig. 15d). Throughout this cycling, A1 experienced very little storm-relative motion. Analyses of dual-Doppler storm-relative streamlines from 0209 to 0218 UTC show that A1 was in virtually zero storm-relative flow, whereas the cyclonic circulations were embedded in strong midlevel rearward storm-relative flow (Fig. 21). The interplay between these midlevel circulations and the low-level (~ 600 m AGL) vorticity field was complicated, with strong associations between the two at times when the midlevel circulation was above a "pool" of weak cyclonic vorticity, resulting in a column of

enhanced vorticity traveling rearward. As the circulations migrated substantially farther rearward in the storm, they became predominantly elevated features. Vertical vorticity maxima often reformed at low levels in a preferred storm-relative location within the hook echo (generally northwest of the anticyclonic vortex). The storm's inability to develop a deep and coherent cyclonic vortex for any appreciable amount of time during its posttornadic phase despite the favorable storm environment is interesting and will be the subject of future work.

8. Summary and conclusions

In this study, we analyzed a nontornadic and a tornadic supercell intercepted by VORTEX2 on 10 June 2010, and compared the interactions with other convective features, the storm environments, kinematic evolution, and outflow strengths. The goal was to
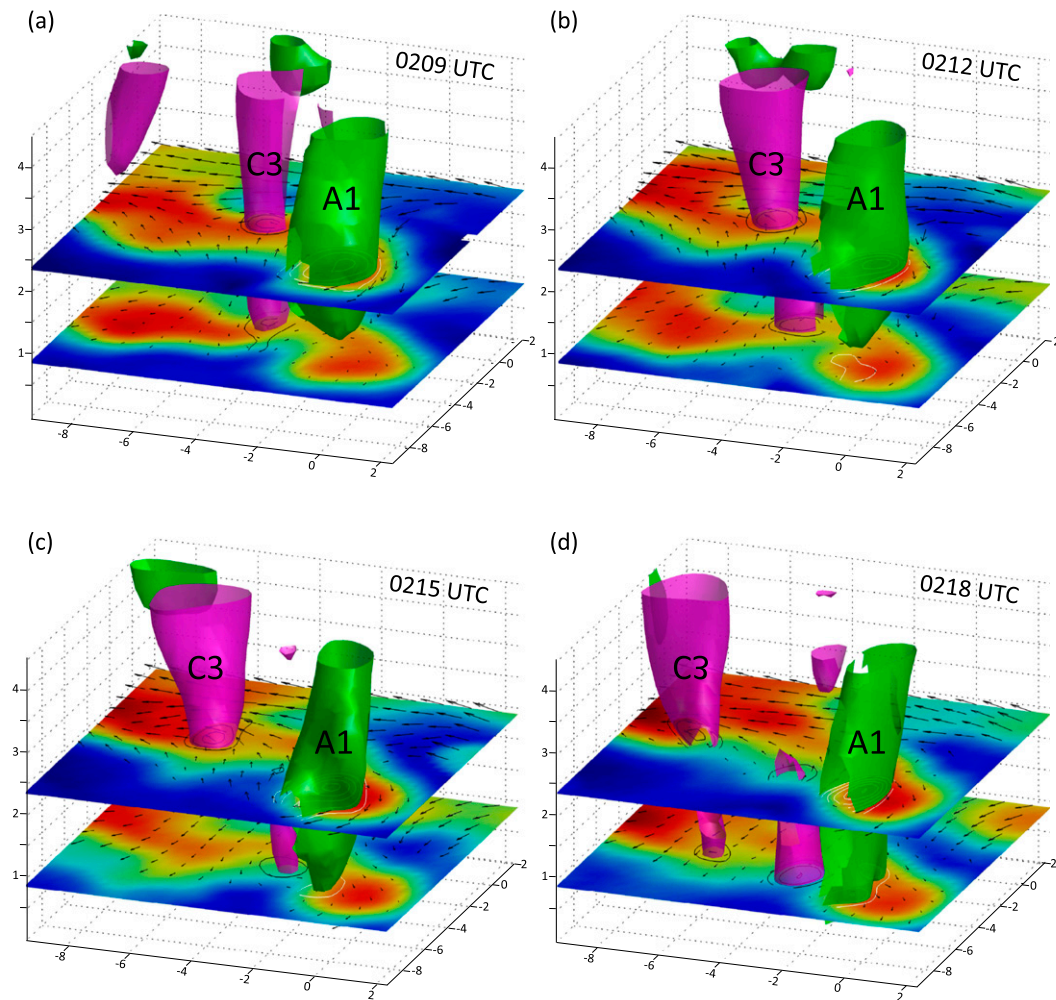
FIG. 21. Dual-Doppler-derived fields in the tornadic supercell during its later, nontornadic phase. Vorticity contours are black (cyclonic vorticity) and white (anticyclonic vorticity), every $0.5 \times 10^{-2}\,\mathrm{s}^{-1}$ beginning at $\pm 1 \times 10^{-2}\,\mathrm{s}^{-1}$. Vorticity isosurfaces are $\pm 1.3 \times 10^{-2}\,\mathrm{s}^{-1}$. Only relevant vorticity features are shown. Objectively analyzed Z_e and storm-relative horizontal wind vectors are shown at 2.4 and 0.9 km.

identify differences and use these to hypothesize why one supercell never produced a tornado and the other produced at least two. Additionally, for the tornadic supercell, the evolution of the two tornadoes and the mesocyclone were studied.

One important difference between the two supercells appeared to be how each interacted with cell A, the storm which initiated between them (Fig. 1). The nontornadic supercell merged with cell A, and this merger led to the demise of the nontornadic supercell by weakening the updraft and mesocyclone through a combination of raining into the updraft and cooling the inflow of the supercell (Fig. 4). Had this merger not happened, would this supercell have been able to produce a tornado? It took the tornadic supercell nearly three hours after initiation to begin producing tornadoes, while the

nontornadic supercell began weakening about two hours into its life. It is likely the nontornadic supercell merely did not have the opportunity to experience the increasingly favorable environment that evolved in time.

Both storms formed in environments that were initially similar and, for the most part, somewhat marginal for the development of tornadoes (especially "significant" tornadoes). The main difference at this early stage was slightly greater low-level storm-relative helicity in the environment of the tornadic supercell (e.g., Fig. 9). As the storms progressed, the environment evolved rapidly, with large increases in both 0–3- and 0–1-km storm-relative helicity and strengthening storm-relative winds, with a reduction of the mixed-layer depth (Fig. 11). While the environment was somewhat heterogeneous from the start, temporal

variations were perhaps even more substantial. Because the environment became increasingly favorable for tornado production in time, the ability of the southern storm to remain isolated (at least with respect to its inflow sector) for a much longer time likely played a critical role in its ability to remain supercellular (Bunkers et al. 2006) long enough to experience these conditions and produce tornadoes.

Comparing the storm attributes, the two storms had cold pools with similar thermodynamic characteristics (at locations/times at which there were data), with outflows that were cold relative to those typical of supercells producing significant tornadoes (e.g., Fig. 16). The nontornadic storm had a significant midlevel mesocyclone but much weaker rotation at low levels. This may be related to the relatively weak storm-relative winds at low levels over most of its lifetime. The tornadic storm, on the other hand, was able to maintain significant low-level rotation (Fig. 15).

The evolution of the two tornadoes and the mesocyclone in the tornadic supercell were also analyzed. During the time period between the two tornadoes, the circulation generally maintained or exceeded tornado strength at most heights, while closer to the surface, the circulation weakened and there was no visible condensation funnel (Fig. 19). The same mesocyclone produced both tornadoes, but after the second tornado, cycling of the mesocyclone occurred. Two new midlevel circulations developed in the rear-flank region and moved rearward relatively quickly aloft. An anticyclonic circulation, on the other hand, remained almost stationary in the hook (Fig. 20). The long nontornadic phase of this storm is puzzling given the increases in STP in its environment. Perhaps the difficulty in producing a deep coherent vortex in a favorable location (i.e., near the main updraft), given the rearward motion of the mesocyclones that did develop, was a critical factor.

Future work will focus on how interactions with cells A and B may have helped the tornadic supercell produce a tornado. To study this, as well as what could have happened in the nontornadic supercell had it not experienced the detrimental merger, model simulations of this case using data assimilation techniques will be performed.

REFERENCES

Alexander, C. R., and J. Wurman, 2005: The 30 May 1998 Spencer, South Dakota, storm. Part I: The structural evolution and environment of the tornadoes. *Mon. Wea. Rev.*, **133**, 72–96, doi:10.1175/MWR-2855.1.

——, and J. M. Wurman, 2008: Updated mobile radar climatology of supercell tornado structures and dynamics. *24th Conf. on Severe Local Storms*, Savannah, GA, Amer. Meteor. Soc., 19.4. [Available online at https://ams.confex.com/ams/pdfpapers/141821.pdf.]

Barnes, S., 1964: A technique for maximizing details in numerical weather-map analysis. *J. Appl. Meteor.*, **3**, 396–409, doi:10.1175/1520-0450(1964)003<0396:ATFMDI>2.0.CO;2.

Beck, J., and C. Weiss, 2013: An assessment of low-level baroclinity and vorticity within a simulated supercell. *Mon. Wea. Rev.*, **141**, 649–669, doi:10.1175/MWR-D-11-00115.1.

Biggerstaff, M., and Coauthors, 2005: The Shared Mobile Atmospheric Research and Teaching radar: A collaboration to enhance research and teaching. *Bull. Amer. Meteor. Soc.*, **86**, 1263–1274, doi:10.1175/BAMS-86-9-1263.

Bolton, D., 1980: The computation of equivalent potential temperature. *Mon. Wea. Rev.*, **108**, 1046–1053, doi:10.1175/1520-0493(1980)108<1046:TCOEPT>2.0.CO;2.

Bothwell, P. D., J. A. Hart, and R. L. Thompson, 2002: An integrated three-dimensional objective analysis scheme in use at the Storm Prediction Center. Preprints, *21st Conf. on Severe Local Storms*, San Antonio, TX, Amer. Meteor. Soc., JP3.1. [Available online at https://ams.confex.com/ams/SLS_WAF_NWP/techprogram/paper_47482.htm.]

Brandes, E., 1977: Flow in severe thunderstorms observed by dual-Doppler radar. *Mon. Wea. Rev.*, **105**, 113–120, doi:10.1175/1520-0493(1977)105<0113:FISTOB>2.0.CO;2.

Bunkers, M. J., M. R. Hjelmfelt, and P. L. Smith, 2006: An observational examination of long-lived supercells. Part I: Characteristics, evolution, and demise. *Wea. Forecasting*, **21**, 673–688, doi:10.1175/WAF949.1.

Burgess, D., V. Wood, and R. Brown, 1982: Mesocyclone evolution statistics. Preprints, *12th Conf. on Severe Local Storms*, San Antonio, TX, Amer. Meteor. Soc., 422–424.

——, E. R. Mansell, C. M. Schwarz, and B. J. Allen, 2010: Tornado and tornadogenesis events seen by the NOXP x-band, dual-polarization radar during VORTEX2 2010. *25th Conf. on Severe Local Storms*, Denver, CO, Amer. Meteor. Soc., 5.2. [Available online at https://ams.confex.com/ams/25SLS/techprogram/paper_176164.htm.]

Coffer, B. E., and M. D. Parker, 2015: Impacts of increasing low-level shear on supercells during the early evening transition. *Mon. Wea. Rev.*, **143**, 1945–1969, doi:10.1175/MWR-D-14-00328.1.

Dahl, J. M. L., M. D. Parker, and L. J. Wicker, 2014: Imported and storm-generated near-ground vertical vorticity in a simulated supercell. *J. Atmos. Sci.*, **71**, 3027–3051, doi:10.1175/JAS-D-13-0123.1.

Davenport, C. E., and M. D. Parker, 2015: Impact of environmental heterogeneity on the dynamics of a dissipating supercell thunderstorm. *Mon. Wea. Rev.*, **143**, 4244–4277, doi:10.1175/MWR-D-15-0072.1.

Davies-Jones, R., 1984: Streamwise vorticity: The origin of updraft rotation in supercell storms. *J. Atmos. Sci.*, **41**, 2991–3006, doi:10.1175/1520-0469(1984)041<2991:SVTOOU>2.0.CO;2.

——, 2008: Can a descending rain curtain in a supercell instigate tornadogenesis barotropically? *J. Atmos. Sci.*, **65**, 2469–2497, doi:10.1175/2007JAS2516.1.

——, 2015: A review of supercell and tornado dynamics. *Atmos. Res.*, **158–159**, 274–291, doi:10.1016/j.atmosres.2014.04.007.

——, and H. Brooks, 1993: Mesocyclogenesis from a theoretical perspective. *The Tornado: Its Structure, Dynamics, Prediction, and Hazards*, *Geophys. Monogr.*, Vol. 79, Amer. Geophys. Union, 105–114.

——, D. W. Burgess, and M. Foster, 1990: Test of helicity as a tornado forecast parameter. Preprints, *16th Conf. on Severe Local Storms*, Kananaskis Park, AB, Canada, Amer. Meteor. Soc., 588–592.

Dowell, D., and H. Bluestein, 2002a: The 8 June 1995 McLean, Texas, storm. Part I: Observations of cyclic tornadogenesis. *Mon. Wea. Rev.*, **130**, 2626–2648, doi:10.1175/1520-0493(2002)130<2626:TJMTSP>2.0.CO;2.

——, and ——, 2002b: The 8 June 1995 McLean, Texas, storm. Part II: Cyclic tornado formation, maintenance, and dissipation. *Mon. Wea. Rev.*, **130**, 2649–2670, doi:10.1175/1520-0493(2002)130<2649:TJMTSP>2.0.CO;2.

——, and A. Shapiro, 2003: Stability of an iterative dual-Doppler wind synthesis in Cartesian coordinates. *J. Atmos. Oceanic Technol.*, **20**, 1552–1559, doi:10.1175/1520-0426(2003)020<1552:SOAIDW>2.0.CO;2.

Finley, C., W. Cotton, and R. S. Pielke, 2001: Numerical simulation of tornadogenesis in a high-precipitation supercell. Part I: Storm evolution and transition into a bow echo. *J. Atmos. Sci.*, **58**, 1597–1629, doi:10.1175/1520-0469(2001)058<1597:NSOTIA>2.0.CO;2.

Frame, J., and P. Markowski, 2013: Dynamical influences of anvil shading on simulated supercell thunderstorms. *Mon. Wea. Rev.*, **141**, 2802–2820, doi:10.1175/MWR-D-12-00146.1.

French, M., H. Bluestein, D. Dowell, L. Wicker, M. Kramar, and A. Pazmany, 2008: High-resolution, mobile Doppler radar observations of cyclic mesocyclogenesis in a supercell. *Mon. Wea. Rev.*, **136**, 4997–5016, doi:10.1175/2008MWR2407.1.

Hastings, R., and Y. Richardson, 2016: Long-term morphological changes in simulated supercells following mergers with nascent supercells in directionally varying shear. *Mon. Wea. Rev.*, **144**, 471–499, doi:10.1175/MWR-D-15-0193.1.

Hirth, B. D., J. L. Schroeder, and C. C. Weiss, 2008: Surface analysis of the rear-flank downdraft outflow in two tornadic supercells. *Mon. Wea. Rev.*, **136**, 2344–2363, doi:10.1175/2007MWR2285.1.

Klemp, J., and R. Rotunno, 1983: A study of the tornadic region within a supercell thunderstorm. *J. Atmos. Sci.*, **40**, 359–377, doi:10.1175/1520-0469(1983)040<0359:ASOTTR>2.0.CO;2.

Koch, S., M. DesJardins, and P. Kocin, 1983: An interactive Barnes objective map analysis scheme for use with satellite and conventional data. *J. Climate Appl. Meteor.*, **22**, 1487–1503, doi:10.1175/1520-0450(1983)022<1487:AIBOMA>2.0.CO;2.

Kost, J., 2004: *Impacts of Temporally Variable Environmental Vertical Wind Shear upon Numerically Simulated Convective Storms.* The Pennsylvania State University, 106 pp.

Lebo, Z. J., and H. Morrison, 2014: Dynamical effects of aerosol perturbations on simulated idealized squall lines. *Mon. Wea. Rev.*, **142**, 991–1009, doi:10.1175/MWR-D-13-00156.1.

Lee, B., B. Jewett, and R. Wilhelmson, 2006: The 19 April 1996 Illinois tornado outbreak. Part II: Cell mergers and associated tornado incidence. *Wea. Forecasting*, **21**, 449–464, doi:10.1175/WAF943.1.

Letkewicz, C. E., A. J. French, and M. D. Parker, 2013: Base-state substitution: An idealized modeling technique for approximating environmental variability. *Mon. Wea. Rev.*, **141**, 3062–3086, doi:10.1175/MWR-D-12-00200.1.

Lilly, D., 1982: The development and maintenance of rotation in convective storms. *Intense Atmospheric Vortices*, L. Bengtsson and J. Lighthill, Eds., Springer-Verlag, 149–160.

Loehrer, S., T. Edmands, and J. Moore, 1996: TOGA COARE upper-air sounding data archive: Development and quality control procedures. *Bull. Amer. Meteor. Soc.*, **77**, 2651–2671, doi:10.1175/1520-0477(1996)077<2651:TCUASD>2.0.CO;2.

——, S. Williams, and J. Moore, 1998: Results from UCAR/JOSS quality control of atmospheric soundings from field projects. Preprints, *10th Symp. on Meteorological Observations and Instrumentation*, Phoenix, AZ, Amer. Meteor. Soc., 1–6.

Majcen, M., P. Markowski, Y. Richardson, D. Dowell, and J. Wurman, 2008: Multipass objective analyses of Doppler radar data. *J. Atmos. Oceanic Technol.*, **25**, 1845–1858, doi:10.1175/2008JTECHA1089.1.

Markowski, P., and Y. Richardson, 2014: The influence of environmental low-level shear and cold pools on tornadogenesis: Insights from idealized simulations. *J. Atmos. Sci.*, **71**, 243–275, doi:10.1175/JAS-D-13-0159.1.

——, J. M. Straka, E. N. Rasmussen, and D. O. Blanchard, 1998: Variability of storm-relative helicity during VORTEX. *Mon. Wea. Rev.*, **126**, 2959–2971, doi:10.1175/1520-0493(1998)126<2959:VOSRHD>2.0.CO;2.

——, ——, and ——, 2002: Direct surface thermodynamic observations within the rear-flank downdrafts of nontornadic and tornadic supercells. *Mon. Wea. Rev.*, **130**, 1692–1721, doi:10.1175/1520-0493(2002)130<1692:DSTOWT>2.0.CO;2.

——, Y. Richardson, M. Majcen, J. Marquis, and J. Wurman, 2011: Characteristics of the wind field in three nontornadic low-level mesocyclones observed by the Doppler on Wheels radars. *Electron. J. Severe Storms Meteor.*, **6**, 1–48.

——, and Coauthors, 2012: The pretornadic phase of the Goshen County, Wyoming, supercell of 5 June 2009 intercepted by VORTEX2. Part I: Evolution of kinematic and surface thermodynamic fields. *Mon. Wea. Rev.*, **140**, 2887–2915, doi:10.1175/MWR-D-11-00336.1.

Marquis, J., Y. Richardson, P. Markowski, D. Dowell, and J. Wurman, 2012: Tornado maintenance investigated with high-resolution dual-Doppler and EnKF Analysis. *Mon. Wea. Rev.*, **140**, 3–27, doi:10.1175/MWR-D-11-00025.1.

NCDC, 2010: *Storm Data.* Vol. 52, No. 6, 1022 pp. [Available from National Centers for Environmental Information, 151 Patton Ave., Asheville, NC 28801-5001.]

NOAA, 2011: 2011 tornado information. Accessed 7 December 2013. [Available online at http://www.noaanews.noaa.gov/2011_tornado_information.html.]

Oye, R., C. Mueller, and S. Smith, 1995: Software for radar translation, visualization, editing, and interpolation. Preprints, *27th Conf. on Radar Meteorology*, Vail, CO, Amer. Meteor. Soc., 359–361.

Parker, M. D., 2014: Composite VORTEX2 supercell environments from near-storm soundings. *Mon. Wea. Rev.*, **142**, 508–529, doi:10.1175/MWR-D-13-00167.1.

——, and J. M. L. Dahl, 2015: Production of near-surface vertical vorticity by idealized downdrafts. *Mon. Wea. Rev.*, **143**, 2795–2816, doi:10.1175/MWR-D-14-00310.1.

Pauley, P., and X. Wu, 1990: The theoretical, discrete, and actual response of the Barnes objective analysis scheme for one- and two-dimensional fields. *Mon. Wea. Rev.*, **118**, 1145–1164, doi:10.1175/1520-0493(1990)118<1145:TTDAAR>2.0.CO;2.

Rasmussen, E., 2003: Refined supercell and tornado forecast parameters. *Wea. Forecasting*, **18**, 530–535, doi:10.1175/1520-0434(2003)18<530:RSATFP>2.0.CO;2.

——, and D. Blanchard, 1998: A baseline climatology of sounding-derived supercell and tornado forecast parameters. *Wea. Forecasting*, **13**, 1148–1164, doi:10.1175/1520-0434(1998)013<1148:ABCOSD>2.0.CO;2.

Richardson, Y. P., and K. K. Droegemeier, 1996: An investigation of the dynamics governing organized multicell rotation and transition. Preprints, *18th Conf. on Severe Local Storms*, San Francisco, CA, Amer. Meteor. Soc., 195–199.

——, ——, and R. P. Davies-Jones, 2007: The influence of horizontal environmental variability on numerically simulated convective storms. Part I: Variations in vertical shear. *Mon. Wea. Rev.*, **135**, 3429–3455, doi:10.1175/MWR3463.1.

Rilling, R., and C. Schumacher, 2013: SMART-R during DYNAMO: A technique to diagnose elevation angle errors. *36th Conf. on Radar Meteorology*, Breckenridge, CO, Amer. Meteor. Soc., P238.

Rogers, J., 2012: Significant tornado events associated with cell mergers. *26th Conf. on Severe Local Storms*, Nashville, TN, Amer. Meteor. Soc., 9.4. [Available online at https://ams.confex.com/ams/26SLS/webprogram/Paper211575.html.]

——, and C. Weiss, 2008: The association of cell mergers with tornado occurrence. *24th Conf. on Severe Local Storms*, Savannah, GA, Amer. Meteor. Soc., P3.23. [Available online at https://ams.confex.com/ams/pdfpapers/141784.pdf.]

Rotunno, R., 1981: On the evolution of thunderstorm rotation. *Mon. Wea. Rev.*, **109**, 577–586, doi:10.1175/1520-0493(1981)109<0577:OTEOTR>2.0.CO;2.

——, and J. Klemp, 1985: On the rotation and propagation of simulated supercell thunderstorms. *J. Atmos. Sci.*, **42**, 271–292, doi:10.1175/1520-0469(1985)042<0271:OTRAPO>2.0.CO;2.

Schenkman, A. D., M. Xue, and M. Hu, 2014: Tornadogenesis in a high-resolution simulation of the 8 May 2003 Oklahoma City supercell. *J. Atmos. Sci.*, **71**, 130–154, doi:10.1175/JAS-D-13-073.1.

Shabbott, C. J., and P. M. Markowski, 2006: Surface in situ observations within the outflow of forward-flank downdrafts of supercell thunderstorms. *Mon. Wea. Rev.*, **134**, 1422–1441, doi:10.1175/MWR3131.1.

Skinner, P. S., C. C. Weiss, P. M. Markowski, and Y. P. Richardson, 2010: Intercomparison between mobile and stationary surface observing platforms in VORTEX2. *25th Conf. on Severe Local Storms*, Denver, CO, Amer. Meteor. Soc., P5.1. [Available online at https://ams.confex.com/ams/25SLS/techprogram/paper_176245.htm.]

——, ——, J. L. Schroeder, L. J. Wicker, and M. I. Biggerstaff, 2011: Observations of the surface boundary structure within the 23 May 2007 Perryton, Texas, supercell. *Mon. Wea. Rev.*, **139**, 3730–3749, doi:10.1175/MWR-D-10-05078.1.

——, ——, M. M. French, H. B. Bluestein, P. M. Markowski, and Y. P. Richardson, 2014: VORTEX2 observations of a low-level mesocyclone with multiple internal rear-flank downdraft momentum surges in the 18 May 2010 Dumas, Texas, supercell. *Mon. Wea. Rev.*, **142**, 2935–2960, doi:10.1175/MWR-D-13-00240.1.

Straka, J. M., E. N. Rasmussen, and S. E. Fredrickson, 1996: A mobile mesonet for fine-scale meteorological observations. *J. Atmos. Oceanic Technol.*, **13**, 921–936, doi:10.1175/1520-0426(1996)013<0921:AMMFFM>2.0.CO;2.

Tanamachi, R. L., H. B. Bluestein, J. B. Houser, S. J. Frasier, and K. M. Hardwick, 2012: Mobile, X-band, polarimetric Doppler radar observations of the 4 May 2007 Greensburg, Kansas, tornadic supercell. *Mon. Wea. Rev.*, **140**, 2103–2125, doi:10.1175/MWR-D-11-00142.1.

——, P. L. Heinselman, and L. J. Wicker, 2015: Impacts of a storm merger on the 24 May 2011 El Reno, Oklahoma, tornadic supercell. *Wea. Forecasting*, **30**, 501–524, doi:10.1175/WAF-D-14-00164.1.

Thompson, R., R. Edwards, and J. Hart, 2002: Evaluation and interpretation of the supercell composite and significant tornado parameters at the Storm Prediction Center. *21st Conf. on Severe Local Storms*, San Antonio, TX, Amer. Meteor. Soc., J3.2. [Available online at https://ams.confex.com/ams/SLS_WAF_NWP/techprogram/paper_46942.htm.]

——, ——, and ——, 2003: Close proximity soundings within supercell environments obtained from the Rapid Update Cycle. *Wea. Forecasting*, **18**, 1243–1261, doi:10.1175/1520-0434(2003)018<1243:CPSWSE>2.0.CO;2.

——, B. Smith, J. Grams, A. Dean, and C. Broyles, 2012: Convective modes for significant severe thunderstorms in the contiguous United States. *Wea. Forecasting*, **27**, 1136–1154, doi:10.1175/WAF-D-11-00116.1.

Trapp, R., and C. Doswell, 2000: Radar data objective analysis. *J. Atmos. Oceanic Technol.*, **17**, 105–120, doi:10.1175/1520-0426(2000)017<0105:RDOA>2.0.CO;2.

——, G. Stumpf, and K. Manross, 2005: A reassessment of the percentage of tornadic mesocyclones. *Wea. Forecasting*, **20**, 680–687, doi:10.1175/WAF864.1.

Waugh, S., and S. E. Fredrickson, 2010: An improved aspirated temperature system for mobile meteorological observations, especially in severe weather. *25th Conf. on Severe Local Storms*, Denver, CO, Amer. Meteor. Soc., P5.2. [Available online at https://ams.confex.com/ams/25SLS/techprogram/paper_176205.htm.]

Weiss, C., and J. Schroeder, 2008: StickNet: A new portable, rapidly deployable surface observation system. *Bull. Amer. Meteor. Soc.*, **89**, 1502–1503.

——, D. C. Dowell, J. L. Schroeder, P. S. Skinner, A. E. Reinhart, P. M. Markowski, and Y. P. Richardson, 2015: A comparison of near-surface buoyancy and baroclinity across three VORTEX2 supercell intercepts. *Mon. Wea. Rev.*, **143**, 2736–2753, doi:10.1175/MWR-D-14-00307.1.

Wurman, J., J. Straka, E. Rasmussen, M. Randall, and A. Zahrai, 1997: Design and deployment of a portable, pencil-beam, pulsed, 3-cm Doppler radar. *J. Atmos. Oceanic Technol.*, **14**, 1502–1512, doi:10.1175/1520-0426(1997)014<1502:DADOAP>2.0.CO;2.

——, Y. Richardson, C. Alexander, S. Weygandt, and P. F. Zhang, 2007: Dual-Doppler and single-Doppler analysis of a tornadic storm undergoing mergers and repeated tornadogenesis. *Mon. Wea. Rev.*, **133**, 97–119, doi:10.1175/MWR3276.1.

——, D. Dowell, Y. Richardson, P. Markowski, E. Rasmussen, D. Burgess, L. Wicker, and H. Bluestein, 2012: The second Verification of the Origins of Rotation in Tornadoes Experiment. *Bull. Amer. Meteor. Soc.*, **93**, 1147–1170, doi:10.1175/BAMS-D-11-00010.1.